Eur. Phys. J. C (2025) 85:1019
https://doi.org/10.1140/epjc/s10052-025-14779-6

THE EUROPEAN
PHYSICAL JOURNAL C

Regular Article - Theoretical Physics

Accretion dynamics and QPO signatures around quantum-corrected black hole: a comparison with Kerr spacetime

O. Donmez[a]

College of Engineering and Technology, American University of the Middle East, 54200 Egaila, Kuwait

Received: 12 July 2025 / Accepted: 8 September 2025

Abstract By numerically solving the general relativistic hydrodynamics (GRH) equations, we investigate quasi-periodic oscillations (QPOs) and accretion dynamics around quantum-corrected black holes (QCBHs). Using the Bondi–Hoyle–Lyttleton (BHL) accretion framework in a quantum-corrected spacetime, we analyze how the black hole spin parameter a/M and the quantum correction parameter b influence the shock cone structure, mass accretion rate, and oscillatory behavior of the surrounding plasma. Our results show that although the shock cone forms in every model, its symmetry, geometry, and opening angle are highly sensitive to both parameters. QPO signals extracted from the mass accretion rate at different radial positions reveal the presence of both low-frequency (LFQPOs) and high-frequency QPOs (HFQPOs). In particular, we confirm that oscillation modes such as f_{EH}, f_{sh}, and f_{LT} are trapped inside the cone, with amplitudes and coherence properties that vary systematically with the parameters. While QCBHs share many QPO signatures with classical Kerr black holes, quantum corrections suppress peak amplitudes near the horizon, shift the QPO-generating regions outward, and preserve recognizable resonance patterns such as the $3:2$ frequency ratio. These results, consistent with both theoretical predictions and observational findings, demonstrate that QCBHs retain key observable features while incorporating quantum gravitational effects. Our findings highlight QPOs as a novel probe of quantum gravity, with implications for future high-resolution observations by the Event Horizon Telescope (EHT) and X-ray binaries (XRBs).

Contents

1 Introduction

Black holes are among the most extreme objects in the universe, generating strong gravitational fields and representing one of the most striking consequences of Einstein's theory of general relativity (GR). These objects, from which even light cannot escape once it reaches the event horizon, have become a major focus of theoretical and observational astrophysics in recent decades. The black holes are formed either as the end state of massive stars undergoing supernova explosions or through the mergers of compact objects in dense astrophysical environments [1,2]. GR does not describe gravity as a conventional force, but rather as the curvature of spacetime induced by mass and energy. The theory predicts the existence of singularities, frame dragging, and relativistic time dilation near the rotating black holes [3]. In recent years, groundbreaking observational efforts, such as the detection of gravitational waves by LIGO and Virgo [2,4], and the

---

[a] e-mail: orhan.donmez@aum.edu.kw (corresponding author)

imaging of the black hole shadow by the EHT [5–9], have provided compelling evidence supporting the existence of the black holes. These discoveries not only confirm key predictions of GR, but also offer a path forward in probing the properties of strong gravitational fields and exploring attempts to unify GR with the laws of quantum physics [10].

Although GR has been highly successful in describing phenomena within the solar system and on astrophysical scales, it has proven insufficient in explaining certain observations. As a result, the development of alternative theories of gravity has become necessary. For instance, the accelerated expansion of the universe [11], the flat rotation curves of galaxies [12], and the formation of large-scale structures cannot be fully explained without invoking dark matter and dark energy. Although these remain central topics in modern cosmology and have been actively investigated both theoretically and observationally, their fundamental nature is still unknown. Moreover, the unification of GR with quantum field theory remains unresolved, as GR is non-renormalizable and breaks down at the Planck scale [13]. To address these issues, various alternative theories of gravity have been proposed, such as $f(R)$ gravity [14], scalar–tensor theories [15], Gauss–Bonnet and Lovelock gravity [16], and the more recent models $f(Q, T)$ and $f(R, T)$ [17]. These theories extend the Einstein–Hilbert action by incorporating higher-order curvature invariants, non-minimal couplings, and additional degrees of freedom like torsion or non-metricity. Beyond explaining dark energy and dark matter phenomena, these modified gravity theories have also been used to model the shadow of the black holes and interaction with matter in the strong gravitational fields, aiming to match observations such as X-ray spectra and the black hole shadows. In addition, they attempt to explain quantum effects such as Hawking radiation, which emerge in high-curvature regimes, thus bridging GR with quantum mechanics [18]. Furthermore, these theories contribute to the broader effort of grand unification, accelerating research in fundamental physics and enabling the proposal of new theoretical frameworks [19].

GR describes the gravitational field around the black holes as a curvature of spacetime, confirms the existence of singularities, and defines the location of the event horizon based on the black hole spin parameter. However, GR also predicts regions, such as the singularity where physical laws break down. This breakdown signals the need for a theory that incorporates quantum effects into gravity. Phenomena such as black hole singularities, event horizons, and Hawking radiation [20] require a more complete framework, as semi-classical approaches are insufficient to fully explain them. Therefore, resolving the singularity problem, understanding the black hole evaporation and information loss, and developing a consistent theory of the black hole thermodynamics necessitate a complete theory of quantum gravity. Various QCBH models have emerged from different quantum gravity frameworks, including string theory [21], loop quantum gravity [22], non-commutative geometry [23], and the generalized uncertainty principle (GUP) approaches [24,25]. These models not only modify the classical black hole metrics but also adjust the Hawking temperature and entropy, and introduce the concept of a minimal length scale. Moreover, quantum-corrected gravity theories such as asymptotically safe gravity [26], effective field theory approaches [27], and $f(R)$-type models with quantum loop corrections [28] offer essential tools to explore the quantum structure of spacetime. Defining or using QCBH models to analyze phenomena in strong gravitational fields is crucial not only to advance our understanding of the black hole physics but also to test quantum gravity theories. These models help to interpret how quantum gravitational effects might manifest in observable data. In this paper, we model physical processes occurring near a QCBH, focusing on its interaction with matter under strong gravitational conditions.

In recent years, the geodesic motion of the test particles around the QCBHs has been extensively studied to understand the influence of the quantum correction parameters on particle trajectories and, consequently, on observable astrophysical phenomena. In these analyses, the black hole and the surrounding spacetime are described using a fixed metric that includes quantum correction terms. The motion of the test particle in this background is then investigated, allowing for the analytical determination of various physical and thermodynamic parameters, including the calculation of QPO frequencies generated by such particles. For instance, in the case of the GUP, the orbits of test particles around the Schwarzschild and the Kerr black holes have been studied to explore how the location of the innermost stable circular orbit (ISCO) changes in the presence of quantum corrections. Orbital frequencies and precession motions of the test particle have also been computed [25,29,30]. Similarly, in loop quantum gravity scenarios, the test of particle dynamics around loop-inspired QCBHs has been used to examine bounded orbits, perihelion precession, and gravitational lensing features relevant for astrophysical observations [31–36]. Moreover, in the noncommutative geometry approach, the motion of test particles around noncommutative-inspired QCBHs has been analyzed to reveal deviations from the classical Kerr case, including detailed studies of redshift and time dilation profiles [23,37,38]. These investigations demonstrate the applicability of the test particle models to QCBHs and provide a theoretical framework for linking quantum gravity effects with observational data around the black holes. The continued study of test particle motion in QCBH spacetime offers valuable opportunities to impose empirical constraints on quantum gravity models and to support theoretical advancements in the field.

The observation of X-ray emissions generated near the event horizon of the black holes due to the accretion of matter offers a valuable opportunity to understand the strong gravitational fields and to compute QPO frequencies. In GR, QPOs are typically modeled using relativistic precession frameworks or through the analysis of epicyclic frequencies. With the emergence of QCBH models, recent studies have extended QPO analyses to such spacetime, revealing both the influence of quantum effects and deviations from the classical GR predictions. One significant line of research involves calculating orbital, radial, and vertical epicyclic frequencies around GUP-corrected black holes. The results indicate that the location of the ISCO shifts due to the quantum corrections, which in turn alters the HFQPOs [39–41]. Similar behavior has been observed in models based on loop quantum gravity, where modifications to the black hole geometry produce parallel changes in the QPO structure [42–45]. Moreover, in scenarios where noncommutative geometry dominates, it has been shown that QPO frequencies are modified by the corresponding quantum parameters [46–48]. Therefore, studying QPOs around QCBHs can serve as a powerful probe for exploring the phenomenology of quantum gravity and testing its predictions against observational data.

Motivated by the importance of identifying QPOs around the QCBHs and understanding their physical origins as a means of probing quantum gravity, this study first investigates the formation of plasma and shock cone structures resulting from BHL accretion onto a QCBH. The effects of key QCBH parameters, namely the black hole spin and the quantum correction term, on these physical structures are examined and discussed in detail. Subsequently, the oscillatory behavior of the accreted matter and the shock cone induced by these effects is analyzed numerically through QPO diagnostics. The resulting QPO patterns, obtained for the first time numerically in a QCBH environment, are then compared to those arising in classical black hole spacetimes under GR. This comparison allows for a thorough discussion of how quantum correction terms influence the nature and frequency of QPOs. Finally, the results of the numerical simulations are compared with both observational data and analytic solutions derived from the motion of the test particles, offering a comprehensive assessment of the physical consistency and implications of the QCBH models.

The organization of this paper is as follows: in Sect. 2, after briefly presenting the GRH equations, we define the quantum-corrected spacetime metric and, accordingly, the lapse function and the shift vector. Next, we briefly explain the theoretical origin of QPO oscillations. In order to demonstrate the necessity of the numerical results, we discuss the astrophysical motivation in Sect. 3. In Sect. 4, we first define the initial and boundary conditions required to numerically solve the GRH equations and to simulate accretion around a QCBH using the BHL accretion mechanism. Then, we investigate the structure of the accretion disk formed around the black hole as a function of different spin parameters and quantum correction parameters. Subsequently, we discuss in detail how the physical structure around the black hole changes with respect to these parameters. Based on the resulting physical mechanism, we identify the trapped oscillation modes and the corresponding QPO frequencies and analyze their dependence on the spin parameter a/M and the quantum correction parameter b. In addition, we examine how the mass accretion rate varies with these parameters. Finally, in Sect. 6, we discuss the obtained results and their agreement with observations in detail, and demonstrate how the numerical findings can explain phenomena occurring in strong gravitational fields. Throughout the paper, geometrized units with $G = c = 1$ are used.

2 Theoretical framework

2.1 GRHD equations

In this study, we numerically solve the GRH equations within the quantum-corrected spacetime metric, assuming an ideal gas equation of state. This framework allows us to model both the formation of the shock cone resulting from BHL accretion to examine the effect of the quantum correction term and also to reveal the QPOs that arise either from matter trapped inside the shock cone or due to the strong gravitational influence of the black hole. To apply high-resolution numerical methods, the GRH equations are first cast into conservation form. The conservation form of the GRH equations follows the formulation presented in [49–51].

$$\frac{\partial U}{\partial t} + \frac{\partial F^r}{\partial r} + \frac{\partial F^\phi}{\partial \phi} = S. \tag{2.1}$$

In this formulation, U, F^r, F^ϕ, and S denote the conserved variable vector, the radial flux vector, the azimuthal flux vector, and the source vector, respectively. These vectors are expressed in terms of the primitive variables (ρ, v^i, p) as follows:

$$U = \begin{pmatrix} D \\ S_j \\ \tau \end{pmatrix} = \begin{pmatrix} \sqrt{\gamma} W \rho \\ \sqrt{\gamma} h \rho W^2 v_j \\ \sqrt{\gamma}(h \rho W^2 - P - W\rho) \end{pmatrix}. \tag{2.2}$$

Here, v_j denotes the three-velocity, which is defined in terms of the four-velocity and other spacetime variables as $v^i = u^i/W + \beta^i/\alpha$. The quantities α and β^i correspond to the lapse function and the shift vector, respectively, and are specified below for the quantum corrected metric. The three-velocity is measured in the Eulerian reference frame. The index positions (upper or lower) can be converted using the spatial three-metric $\gamma_{i,j}$. The Lorentz factor is given by $W = (1 - \gamma_{a,b} v^i v^j)^{1/2}$, and γ denotes the determinant of the spatial metric. The specific enthalpy is defined as $h = 1 + \epsilon + P/\rho$. Based on these primitive and conservative variables, the corresponding fluxes and source terms are expressed as follows [52]:

$$F^r = \begin{pmatrix} \alpha\left(v^r - \frac{\beta^r}{\alpha}\right) D \\ \alpha\left(\left(v^r - \frac{\beta^r}{\alpha}\right) S_j + \sqrt{\gamma} P \delta^r_j\right) \\ \alpha\left(\left(v^r - \frac{\beta^r}{\alpha}\right) \tau + \sqrt{\gamma} P v^r\right) \end{pmatrix}, \tag{2.3}$$

$$F^\phi = \begin{pmatrix} \alpha\left(v^\phi - \frac{\beta^\phi}{\alpha}\right) D \\ \alpha\left(\left(v^\phi - \frac{\beta^\phi}{\alpha}\right) S_j + \sqrt{\gamma} P \delta^\phi_j\right) \\ \alpha\left(\left(v^\phi - \frac{\beta^\phi}{\alpha}\right) \tau + \sqrt{\gamma} P v^\phi\right) \end{pmatrix}, \tag{2.4}$$

and,

$$\vec{S} = \begin{pmatrix} 0 \\ \alpha\sqrt{\gamma} T^{ab} g_{bc} \Gamma^c_{aj} \\ \alpha\sqrt{\gamma}\left(T^{a0}\partial_a \alpha - \alpha T^{ab}\Gamma^0_{ab}\right) \end{pmatrix}, \tag{2.5}$$

where Γ^c_{ab} is the Christoffel symbol.

In modeling the behavior of matter around the black hole, we assume that it behaves as a perfect fluid. Consequently, the equation of state is given by $P = (\Gamma - 1)\rho\epsilon$, where ϵ is the specific internal energy and Γ is the adiabatic index of the fluid. Furthermore, the numerical solution of the GRH equations requires the definition of the spacetime four-metric g_{ab}, the corresponding three-metric $\gamma_{i,j}$, and the Christoffel symbols Γ^c_{ab} in order to characterize the disk structure and other astrophysical processes in the vicinity of the black hole. In this study, we adopt the QCBH metric in Boyer–Lindquist coordinates, which is given by [53,54]

$$\begin{aligned} ds^2 = &-\left(1 - \frac{2M(r)r}{\Sigma}\right) dt^2 - \frac{4aM(r)r\sin^2\theta}{\Sigma} dt d\phi \\ &+ \frac{\Sigma}{\Delta} dr^2 + \Sigma d\theta^2 \\ &+ \left(r^2 + a^2 + \frac{2a^2 M(r) r \sin^2\theta}{\Sigma}\right) \times \sin^2\theta d\phi^2, \end{aligned} \tag{2.6}$$

where $\Delta = r^2 - 2M(r)r + a^2$, $M(r) = M - \frac{bM^4}{2r^3}$, and $\Sigma = r^2 + a^2\cos^2$.

The lapse function α and the shift vector β^i of the quantum-corrected Kerr metric are

$$\begin{aligned} \alpha &= \left(\frac{1 - \frac{2M(r)r}{\Sigma} + \frac{4a^2 M(r)^2 r^2}{\Delta}\left(a^2\Sigma + 2a^2 M(r) r + \Sigma r^2\right)}{\frac{\Sigma^3}{\Delta}\left(a^2\Sigma + 2a^2 M(r) r + \Sigma r^2\right)}\right)^{1/2} \\ \beta^i &= \left(0, 0, -\frac{2M(r)ar}{\Sigma}\right). \end{aligned} \tag{2.7}$$

The curvature of the spacetime metric around the black hole is governed by three parameters: the black hole mass M, the spin parameter a, and the quantum correction parameter b. Since geometrized units are used, the spin parameter a is expressed in terms of M, while b is dimensionless. Depending on the value of these parameters, the black hole may exhibit an event horizon (outer horizon) and a Cauchy horizon (inner horizon), as illustrated in Fig. 1. For the non-rotating black hole case where $a/M = 0$, only the event horizon forms for all values of b. In contrast, for $a/M = 0.5$ and $a/M = 0.9$, both the event horizon and the Cauchy horizon appear. In the case of $a/M = 0.5$, horizons form for all b values less than 1. However, in the case of $a/M = 0.9$, horizons exist only for certain b values (specifically, $b < 0.23$); for larger b, a naked singularity emerges. The presence of a naked singularity does not, in principle, prevent the modeling of accretion disks around such compact objects. However, the disk structure, stability, and observational signatures may differ from those around the black hole [55]. Therefore, in this study, we investigate the behavior of the shock cone and the resulting QPOs that form around the black hole or the naked singularity for different rotation parameters, using a fixed value of b.

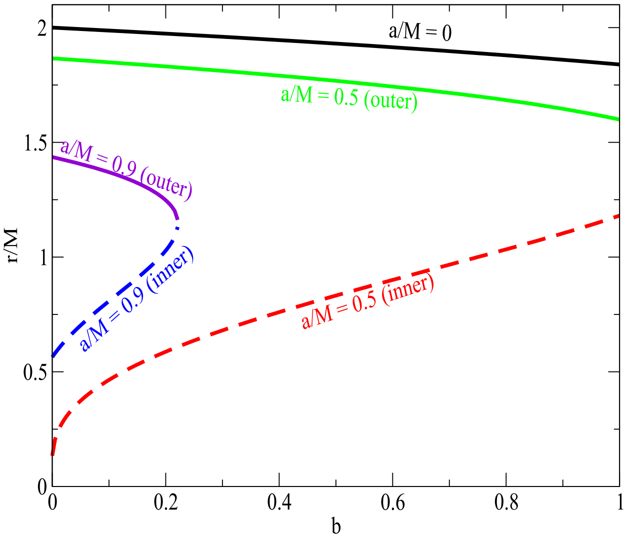

Fig. 1 The variation of the event (outer) and the Cauchy horizon (inner) of the QCBH with respect to the quantum-corrected parameter for different black hole spin parameters has been shown. It has been observed that as the quantum correction parameter increases, the radius of the black hole decreases

2.2 BHL accretion in curved spacetime

The BHL accretion mechanism is important for understanding the dynamic structure of the plasma environment that forms around the black holes and for interpreting high-energy radiation resulting from the black hole-matter interactions in light of observational data. Originally introduced by [56,57], BHL accretion occurs when the black hole moves through a uniform medium, leading to steady-state accretion of matter onto the black hole.

Modeling this accretion process in curved spacetime, resulting from the black hole warping of the surrounding space, is essential for studying astrophysical phenomena that occur in strong gravitational fields. In the classical formulation of the BHL mechanism, matter falls toward a point mass M with an asymptotic velocity V_∞. In this scenario, the accretion radius is given by [58]

$$R_{acc} = \frac{2GM}{V_\infty^2 + C_\infty^2}, \tag{2.8}$$

where C_∞ denotes the sound speed in the medium. The corresponding mass accretion rate is expressed through the equation given as

$$\frac{M_{BHL}}{dt} = \pi R_{acc}^2 \rho_\infty \sqrt{V_\infty^2 + C_\infty^2}. \tag{2.9}$$

These expressions are valid under the assumptions also adopted in this study, which is an adiabatic fluid without magnetic fields.

However, when attempting to study or model BHL accretion in regions near the supermassive black holes, where spacetime curvature is extremely strong, the classical approach becomes insufficient [59]. Instead, we must solve the GRH equations. This allows the effects of spacetime curvature and streamline topology to be incorporated into the calculations. It also enables the understanding of frame dragging, a relativistic effect arising from the black hole spin parameter [60]. These features vary depending on the properties of the curved spacetime used. Numerically, the structure of the resulting shock cone, the QPO generation mechanisms and instabilities such as flip-flop modes can all be studied as functions of the black hole spin and the asymptotic velocity of the ambient medium [61].

In recent years, the application of BHL accretion in the context of modified gravity theories has gained attention, particularly to explain certain astrophysical phenomena and to interpret data from telescopes such as the EHT, which have imaged the black holes such as $M87^*$ and $SgrA^*$ [5–9]. These studies are valuable in exploring how spacetime curvature affects matter inflow, how frame dragging manifests, and in understanding key phenomena such as redshifted accretion luminosity and backreaction effects.

2.3 Theoretical origin of the QPOs

QPOs originate from oscillatory behavior occurring near the black hole event horizon, particularly in the strong gravitational field region where $r < 10M$. These oscillations are generally induced by the black hole-disk interactions [62,63]. Therefore, physical structures that may form in the disk, such as shock waves and shock cones, are of great importance because they influence the QPO frequencies inferred from X-ray observational data [64–67]. Revealing the physical characteristics of these structures is essential.

However, the observation of QPO frequencies can help constrain physical properties of the central black hole, such as its spin parameter and mass, while also providing insight into the nature of gravity itself. QPOs observed around the black holes are generally classified into two categories. LFQPOs typically lie in the frequency range of 0.1–30 Hz. They are most commonly observed in the transient black hole XRBs and are classified as types A, B, and C depending on their coherence and amplitude characteristics. All QPOs observed above 30 Hz fall into the HFQPO category. Observational studies suggest that these frequencies usually originate in regions close to the ISCO.

A foundational approach to understanding QPOs lies in the study of relativistic orbital motion in curved spacetime. In the quantum-corrected spacetime metric, a test particle in a circular equatorial orbit exhibits three characteristic frequencies: the orbital frequency, the radial epicyclic frequency, and the vertical (latitudinal) epicyclic frequency. These frequencies are defined in [36] as:

$$\nu_j = \frac{1}{2\pi}\left(\frac{c^3}{GM}\right)\Omega_j, \tag{2.10}$$

where j denotes r, θ, or ϕ for the radial, vertical, and azimuthal components, respectively, and Ω_j represents the angular frequencies as observed by a distant observer. The explicit forms of Ω_r, Ω_θ, and Ω_ϕ are given in Equations (22), (23), and (24) of [36] for QCBH. Furthermore, the dependence of these frequencies on the black hole spin parameter a and the quantum correction parameter b is discussed in detail, particularly around the ISCO. Additionally, the influence of QCBH parameters on the Lense–Thirring precession frequency is revealed [36], caused by frame dragging near the equatorial plane. Originally proposed by [68], the relativistic precession model (RPM) associates LFQPOs with the Lense–Thirring precession of orbits.

Theoretical studies of relativistic orbital and precession frequencies have been crucial in explaining observed LFQPO and HFQPO behaviors. Moreover, the interaction of hot plasma with strong gravitational fields around the black holes, along with the formation of oscillatory modes trapped in structures such as shock waves and shock cones, are essential in interpreting observational data. Diskoseismology is the study of global oscillation modes trapped in the inner region of the accretion disk around a black hole. These modes are classified according to the dominant restoring force. The first type is the g-modes (inertial-gravity modes), which occur when the motion of the fluid is governed by buoyancy and Coriolis forces. Another type is the p-modes (pressure modes), which arise due to pressure gradients acting as the restoring force. Finally, the c-modes (corrugation modes) originate from the warping of the disk caused by the black hole rotation. These are associated with the frame-dragging effect, known as the Lense–Thirring effect. By analyzing these modes, diskoseismology provides a valuable tool for probing the structure, dynamics, and spacetime geometry in the vicinity of the central object [69–71]. These modes emerge in GRHD simulations as a result of matter dynamics around the black hole. Although these modes are conceptually rich, their detectability in current observational data remains a topic of active debate. At this point, we contribute to solving this problem, understanding the nature of QPOs, and revealing the physical mechanisms responsible for them through the studies presented in this paper.

3 Astrophysical motivation

The QCBHs have several astrophysical motivations. These include enabling the study of singularities in scenarios where a naked singularity might form, improving our understanding of the black hole thermodynamics, and providing a framework for analyzing potential observational signatures of quantum corrections. The classical black holes as described by GR contain singularities. Quantum modifications aim to address these singularities by introducing corrections near or at the event horizon. For instance, quantum gravity effects can lead to nonsingular black hole solutions with a de Sitter core, effectively incorporating quantum corrections and eliminating the classical singularity [72]. Similarly, loop quantum gravity produces the nonsingular black hole solutions by resolving the singularity. This opens the door to studying QPOs occurring around such the black holes, as well as to analyzing gravitational waveforms in the presence of quantum effects [73].

QCBHs, unlike the classical black holes, can exhibit distinct observable features. These include modifications to the black hole shadow and gravitational lensing effects. The quantum correction parameter affects both the lensing characteristics and the Einstein ring. Such effects can manifest in observations as changes in angular position and brightness [74]. Observations of the black hole shadows by EHT [5–9] have already placed constraints on quantum correction parameters. Furthermore, there are proposals on how future telescope designs could differentiate between classical and QCBHs [53,74,75].

Quantum corrections are known to result in slower oscillatory behavior and increased damping of quasi-normal modes. Numerous studies have reported that the real components of quasi-normal modes frequencies tend to decrease, while the absolute values of the imaginary components also diminish as the quantum correction parameter increases [76,77]. These findings indicate that oscillations in the vicinity of the black hole become more gradual and decay more slowly when quantum effects are taken into account. As a result, QCBHs provide a promising theoretical framework for interpreting the LFQPOs detected in astrophysical observations.

It is well known that the QPOs observed in XRBs and active galactic nuclei (AGNs) originate from high-angular-momentum accretion disks around the central black holes of these systems, such as those described by the physical mechanism of Shakura–Sunyaev disks [78]. However, in this work, we analyze QPOs by examining the dynamical structure of the plasma formed through BHL accretion, which possesses small or nearly negligible angular momentum. We can justify this choice for two main reasons. First, the BHL accretion mechanism provides a clean environment around the black hole that primarily leads to the formation of a shock cone. As discussed in the literature [79–81], the shock cone acts as a resonant cavity where oscillation modes can be trapped and excited, allowing us to reveal the influence of the quantum correction parameter on these modes. In particular, the shock cone behaves like a cavity in which velocity and pressure perturbations become trapped between shock locations in azimuthal direction or between the stagnation point and the event horizon [80,82]. Oscillation modes excited in these regions give rise to both LFQPOs and HFQPOs. Importantly, such oscillations are not artifacts of disk physics alone but emerge from the intrinsic hydrodynamic response of the flow to strong gravity, as shown in various studies [79,80]. Therefore, even at low angular momentum, the shock cone represents a robust physical mechanism for the generation of QPOs. Second, previous GRHD simulations have demonstrated that even low-angular-momentum inflows can produce global oscillation modes and, through nonlinear couplings, generate resonance conditions (such as the 3:2 ratio) that are also observed in high-angular-momentum accretion scenarios. Therefore, although our setup does not replicate all features of realistic accretion disks, it does capture the essential QPO-generating mechanisms. In this way, the BHL accretion framework offers us a unique opportunity to study how the quantum correction term influences QPOs around QCBHs. We emphasize that our results should be viewed as complementary to disk-based models, and extending this analysis to thin disks will be an important avenue for future work.

Variations in quasi-normal modes frequencies induced by quantum corrections offer a valuable tool for probing physical processes near the event horizon. For instance, the emergence of overtone outbursts in the quantum Oppenheimer–Snyder black hole model reveals marked deviations from the classical Schwarzschild black holes. These differences may manifest observationally in the form of QPOs [83,84]. Quantum corrections can be tested observationally through QPOs detected in XRBs. For example, QPOs observed in the GRO J1655-40 XRBs have been used to place constraints on the parameters of the loop quantum gravity models [85,86].

Table 1 The initial physical parameters specified in the simulation include the black hole spin parameter a/M and the quantum correction parameter b

a/M	0.9	0.5	0.0
b	0.0 0.1 0.2 0.4 0.6 0.8	0.0 0.1 0.2 0.4 0.6 0.8	0.0 0.1 0.2 0.4 0.6 0.8

4 Simulation results

4.1 Initial conditions

To model the interaction between the black hole and the surrounding plasma, we restrict our simulation to the two-dimensional equatorial plane by setting $\theta = \frac{\pi}{2}$. In this framework, we investigate the formation of a shock cone within a strong gravitational field, arising from the accretion of matter onto QCBH via BHL accretion. The shock cone evolves into a quasi-steady state around $t = 2000M$. To verify that the configuration has truly stabilized and to identify any QPOs, we extend the simulation up to $t = 40{,}000$ M. This long-term evolution confirms that the detected oscillation modes are persistent and not transient artifacts of the system.

During simulation of shock cone formation via BHL accretion, the infall of matter toward the black hole is governed by an asymptotic velocity of $V_\infty = 0.2$. Matter is injected from the outer boundary toward the black hole with prescribed radial and azimuthal velocity components, following the formulation in [52]:

$$V^r = \sqrt{\gamma^{rr}} V_\infty cos(\phi),$$
$$V^\phi = -\sqrt{\gamma^{\phi\phi}} V_\infty sin(\phi). \tag{4.1}$$

Throughout the evolution of the shock cone formation, matter is allowed to accrete onto the black hole with the velocity components specified in Eq. 4.1. The rest-mass density and pressure of the infalling material are chosen to ensure a sound speed of $C_s = 0.1$. To this end, we fix the density at $\rho = 1$. Given this choice, the corresponding pressure is computed using the ideal gas equation of state as

$$P = \frac{C_s^2 \rho(\Gamma - 1)}{\Gamma(\Gamma - 1) - C_s^2 \Gamma}. \tag{4.2}$$

For all numerical calculations, the adiabatic index is set to $\Gamma = 4/3$. The other physical parameters are given in Table 1

The computational domain is discretized using points on the 1024 grid in the radial direction and 512 points in the azimuthal direction. The radial coordinate ranges from $r_{\min} = 2.3M$ to $r_{\max} = 100M$, while the azimuthal coordinate spans the full circle from 0 to 2π. In both this study and previous work, it has been confirmed that the observed QPOs are independent of the numerical resolution.

Outflow boundary conditions are applied in the radial direction at both the inner boundary near the black hole horizon and at the outer edge of the domain. When matter is injected from the upstream side in accordance with the BHL accretion setup, the physical properties of the inflowing material are automatically copied into the ghost zones. These outflow conditions are essential for suppressing the propagation of numerical artifacts into the physical domain containing the disk or plasma. In the azimuthal direction, periodic boundary conditions are imposed to preserve continuity across the angular domain.

4.2 Formation of the accretion disk

The plasma structure formed by BHL accretion around the black holes gives rise to a fundamentally different physical mechanism compared to structures generated by accretion models such as Shakura–Sunyaev. The physical properties of the flow structure formed around the black hole under BHL accretion depend on the asymptotic velocity V_∞ at which the gas is directed toward the black hole, the black hole spin parameter, the equation of state, and possible relativistic effects arising from alternative gravity theories [66,67,79,82,87–94]. In this study, building on our previous work, we examine the morphology of the plasma structure around the QCBH under the assumption of an asymptotic velocity of $V/c = 0.2$ [66,67,79,82,87–91,94], using an ideal gas equation of state and exploring different values of the spin parameter.

As seen in Fig. 2, for each model, including Kerr and those based on alternative gravity theories previously studied, a shock cone forms independently of the quantum correction parameter b and the spin parameter of the black hole. According to the vector plots in Fig. 2, matter falling supersonically from the upstream region toward the black hole gives rise to a detached shock cone in the downstream region. Particularly in the strong gravitational field region $r < 6M$, the spin of the black hole significantly distorts the spacetime, leading to a high-density comet-like structure. The effect of the black hole spin is especially evident when comparing the morphologies of rotating and non-rotating black hole models. This influence becomes clearly visible in regions close to the event horizon. As will be discussed in more detail later, the structure of the shock cone distorted by spacetime curvature turns out to be almost independent of the quantum correction parameter.

In addition, a wake structure is formed in the downstream region, on the opposite side of the black hole from the matter

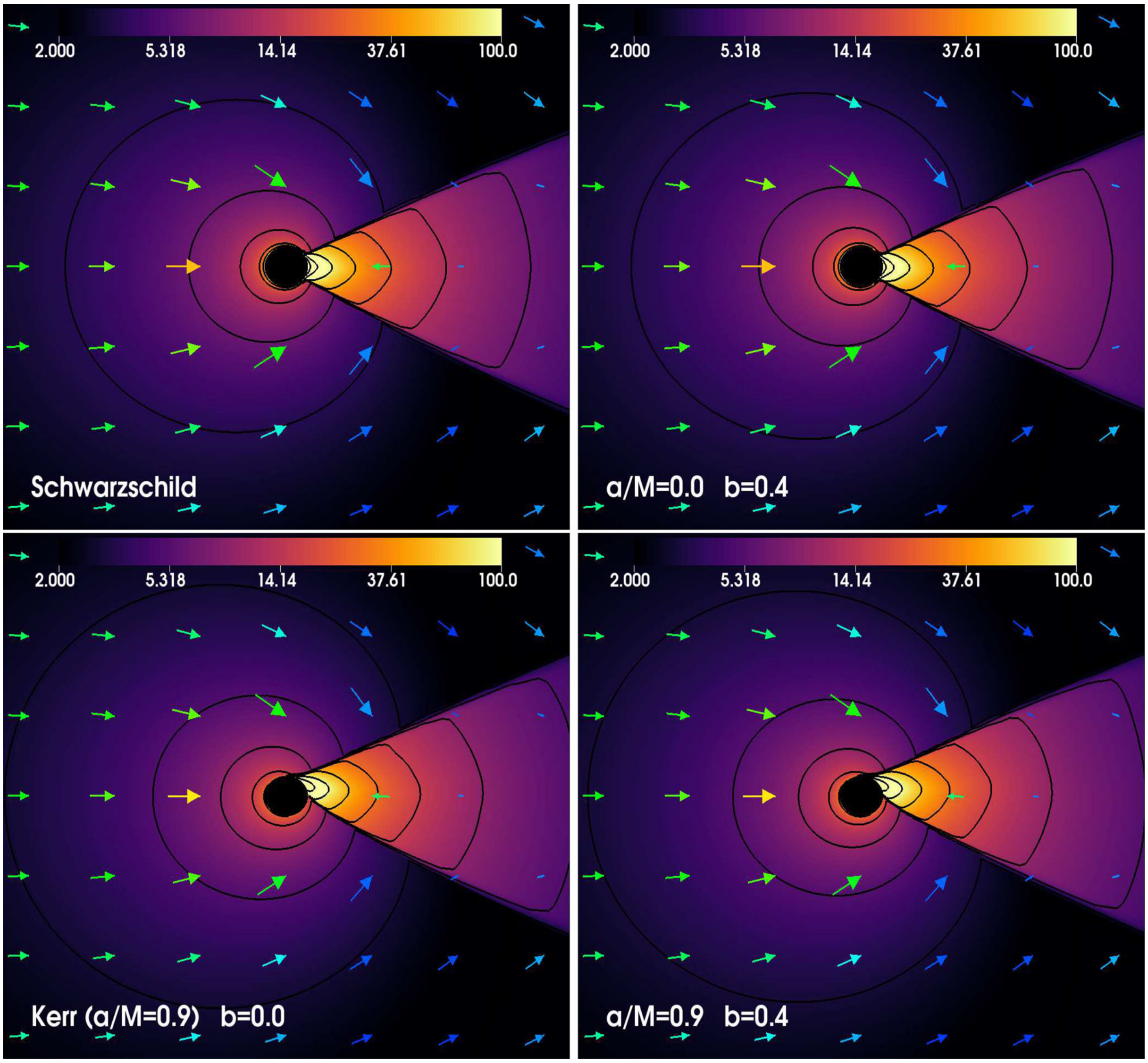

Fig. 2 The variation of the rest-mass density on the equatorial plane is shown using both color and contour plots. The first row presents the density distribution for a non-rotating black hole, comparing the Schwarzschild case with the QCBH for $b = 0.4$. The second row illustrates the behavior for a rotating black hole with a spin parameter of $a = 0.9$, comparing the Kerr and QCBH ($b = 0.4$) cases. In each case, vector plots are included to show the direction of matter flow, highlighting both the BHL infall into the black hole and the flow patterns inside and outside the formed shock cone. To better visualize the changes in the strong gravitational field, the plots are zoomed in with $[x_{max}, y_{max}] = [30M, 30M]$

inflow, extending toward the outer boundary. The shock cone typically forms in relativistic or mildly relativistic regimes. As shown in Figs. 4 and 5, strong shock waves arise at the boundaries of the cone. In this region, matter either exits or enters the cone, leading to sudden changes in the physical variables of matter. Furthermore, as will also be discussed later and seen in Fig. 11, the stagnation point forms within the cone. Matter trapped in the wake region between the stagnation point and the black hole horizon falls through a narrow funnel toward the black hole, continuously feeding it. The wake is typically elongated and axisymmetric, but due to black hole spin and flow instabilities, asymmetries may arise. The shock cone develops Kelvin–Helmholtz and Rayleigh–Taylor instabilities. The structure inside the cone is highly turbulent and exhibits continuous instabilities. Interestingly, the bow shock structure observed in some previous Kerr and alternative gravity models does not appear in QCBH models, even for different values of the quantum correction parameter b.

Numerically determining the mass accretion rate around the black holes is important for understanding the phenomena occurring in the strong gravitational fields. This is because the accretion rate can help explain observable features such as the black hole shadow, variations in X-ray emission, and the formation of QPOs. The brightness observed in X-ray observations is entirely dependent on the magnitude of the mass accretion rate. At the same time, a high mass accretion rate indicates the presence of a hotter environment [95]. These high temperatures lead to changes in the blackbody and Comptonization spectra. The transition between hard and soft X-ray states is entirely governed by the mass accretion rate [96]. The mass accretion rate, which influences such physical processes, is also a physical parameter that explains the jets formed around the black holes in the strong gravitational fields. According to observational results, it has been shown that the power of jets is proportional to the mass accretion rate [97]. Additionally, both the literature and our previous studies have shown that understanding QPO formations and their frequencies is possible through analyzing the accretion rate [98]. The brightness of the black hole shadow revealed by EHT observations and the observed photon density are proportional to the amount of matter falling toward the black hole. Therefore, the accretion of a large amount of matter explains a brighter shadow. For these reasons, modeling the mass accretion rate in the strong gravitational field or the inner disk region is an important task for explaining observational results. In the following, we reveal the effects of a/M, b, and location where the mass accretion rate is calculated in strong gravitational fields (at $r = 2.3M$) and in the inner disk region (very close to the ISCO, at $r = 6.08M$), thus contributing to the interpretation of the observational data.

In Fig. 3, the time evolution of the mass accretion rate resulting from BHL accretion around the QCBH is shown, as a function of the physical parameters. These parameters are a/M, b, and the radial distance. In the top row of Fig. 3, the variation of the mass accretion rate is presented for the rapidly rotating black hole with $a/M = 0.9$, at $r = 2.3M$ (left) and $r = 6.08M$ (right). Compared with the second and third rows of the same figure, the mass accretion rate is seen to be highest at $r = 2.3M$ for $a/M = 0.9$. However, the fluctuations are mild, indicating a more steady-state behavior. As b increases, the mass accretion rate increases systematically. In this case, it is observed that the Kerr black hole (i.e., without quantum correction) has the lowest accretion rate. Therefore, it is numerically confirmed that, in the case of the rapidly rotating black hole in a strong gravitational field, b significantly increases the mass accretion rate. However, for the same $a/M = 0.9$ at $r = 6.08M$, as expected, the mass accretion rate is observed to decrease significantly. In this case, the fluctuations are larger, suggesting that the behavior in this region is more turbulent and unstable.

On the other hand, for a moderately rotating black hole with $a/M = 0.5$, shown in the middle row of Fig. 3, the accretion rate at $r = 2.3M$ is lower than for $a/M = 0.9$, but higher than at $r = 6.08M$. Although increasing b still leads to slightly higher mass accretion at $r = 2.3M$, it is observed that b does not significantly affect the mass accretion rate at $r = 6.08M$. In the case of the non-rotating black hole shown in the bottom row of Fig. 3, the mass accretion rates are much lower compared to the rotating black hole cases, and the accretion rate exhibits strong fluctuations. In this case, it can be said that b has almost no effect on the mass accretion rate.

In conclusion, a rapidly rotating black hole leads to a higher mass accretion rate and more stable behavior in the strong gravitational field. The reason is the strong frame-dragging effect, which supports the transfer of angular momentum and thus leads to a more stable mass accretion. However, while the stronger gravitational field near the black hole promotes a more stable structure, the inner disk region (around $r = 6.08M$) exhibits more turbulent and noisy accretion behavior. This is due to the shock wave interactions and weaker gravitational forces in that region. Finally, it is observed that large values of b, especially when combined with a high spin parameter, significantly increase the mass accretion rate. The reason for this is that a large b value, together with a large a/M, enhances the gravitational attraction and thus modifies the curvature of spacetime.

4.3 Shock cone evolution

Revealing the dependence of plasma and shock cone structures that form in the strong gravitational field of a QCBH on the parameters that define the geometry of the black hole and spacetime can provide explanations both for the black hole shadows observed by the EHT and for the physical mechanisms underlying QPOs identified in data from X-ray telescopes. In this section, we specifically investigate how the structure of the shock cone in strong gravitational fields depends on these parameters.

Figure 4 shows the variation of the rest-mass density along the azimuthal direction at $r = 2.6M$ and $r = 6.08M$ around the black hole. As can be seen in the left panel of Fig. 4, the density distribution of the shock cone exhibits a sharp peak. This peak arises entirely due to the relativistic effects acting on the supersonically infalling matter toward the black hole. It can be said that the shock cone around the Kerr black hole is slightly narrower compared to that of the QCBH. As the quantum correction parameter b increases, the peak density increases slightly. Additionally, the opening angle of the shock cone shows a small increase with increasing b. Furthermore, with higher b values, the curvature of the cone becomes more symmetric and smoother, implying that quantum corrections alter the spacetime geometry. Therefore, it is inferred that b slightly modifies the structure of the shock cone, and this change originates from the spacetime deformation due to the quantum correction term.

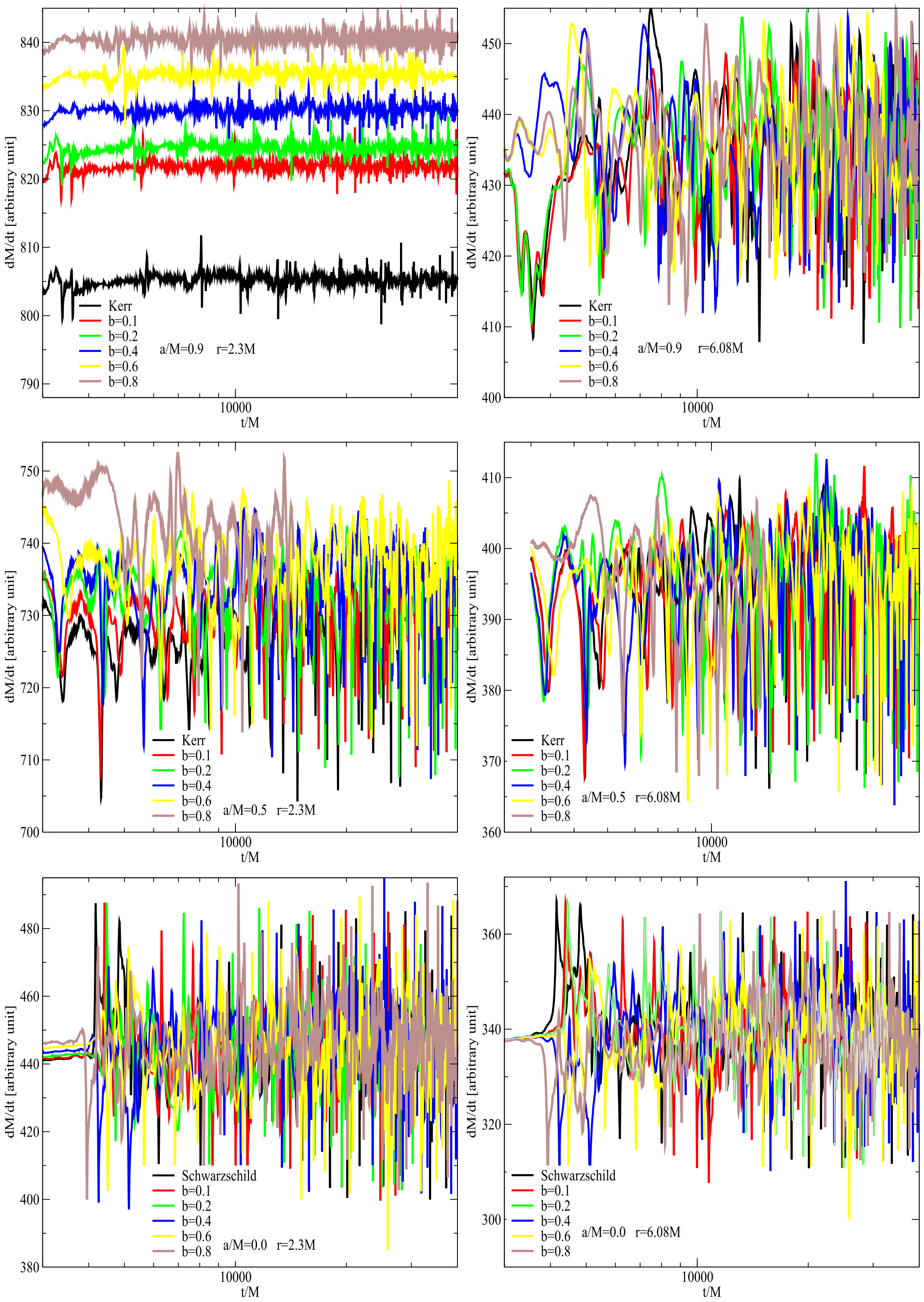

Fig. 3 The variation of the rest-mass density accretion rate over time, depending on different quantum correction parameters b, is shown. The mass accretion rate is calculated at $r = 2.3M$ and $r = 6.08M$ for different values of the rotation parameter. The first and second rows present the mass accretion rate at different radial distances for the rotating black holes with $a = 0.9$ and $a = 0.5$, while the third row shows the same situation for the non-rotating black hole with $a = 0.0$. After the shock cone formed around the black hole reaches a steady state, it is observed that the mass accretion rate exhibits fluctuations around a certain value

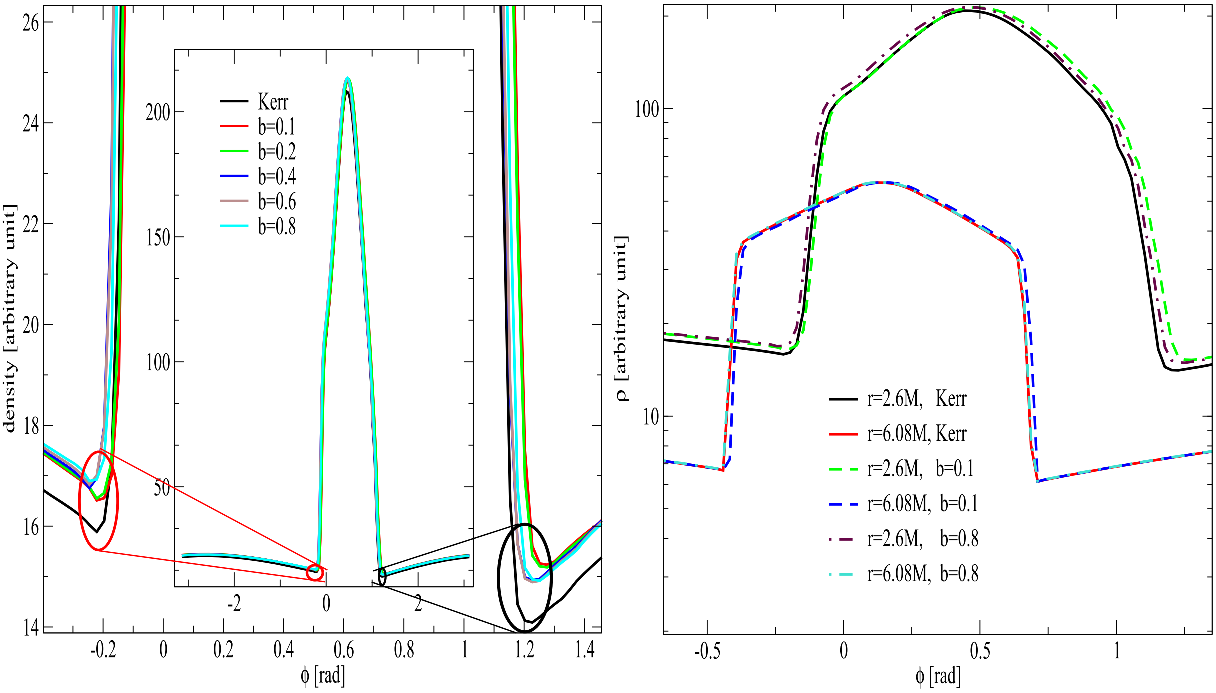

Fig. 4 For a rapidly rotating black hole with $a/M = 0.9$, the variation of the rest-mass density in the azimuthal direction around the black hole is shown for different values of b. The left panel illustrates the structure of the shock cone at $r = 2.6M$ for various values of b, while the right panel shows the shock cone structure at both $r = 2.6M$ and $r = 6.08M$ for the same set of b values. In these figures, the curvature of the shock cone due to spacetime bending is clearly revealed, and it is shown that the opening angle of the cone changes with increasing b when compared to the Kerr case

In the right panel of Fig. 4, the azimuthal variation of the rest-mass density is compared for $r = 2.6M$ and $r = 6.08M$, for both $b = 0.1$ and $b = 0.8$. As expected, the density at $r = 6.08M$ is lower and the boundaries of the shock cone are sharper and more symmetric. In contrast, at $r = 2.6M$, due to the stronger gravitational force, the cone is broader and the density higher. Increasing b leads to a widening of the cone, and this effect is more pronounced at $r = 2.6M$, where the gravitational field is stronger. However, the widening of the cone is relatively weaker at $r = 6.08M$. The radial distance r affects both the density amplitude and the sharpness of the shock; the closer to the black hole, the more compact and intense the shock features. The parameter b modulates the shock behavior more effectively in regions of strong gravitational fields.

One of the most striking features in the right panel of Fig. 4 is the asymmetric distribution of density due to the high frame-dragging effect resulting from $a/M = 0.9$. In this case, the leading part of the shock cone forms slightly off-axis. Therefore, frame dragging enhances mass inflow on the prograde side, creating coherent and directional density enhancements. Changes in the structure of the shock cone due to the parameters a and b directly induce oscillations, which facilitate the formation of QPOs. A narrow and sharply defined cone supports coherent QPOs. As b increases, the cone becomes wider, potentially leading to more turbulence inside the cone, which can modify QPO frequencies and coherence properties. Furthermore, a broader shock cone resulting from higher b values results in smoother emission, which in turn can lead to asymmetry in the black hole shadow and increased brightness in the photon ring region.

As in Fig. 4, in Fig. 5 we examine the azimuthal variation of the rest-mass density at the same radii to reveal the effect of the quantum correction parameter b in a strong gravitational field for the non-rotating black hole. The left panel of Fig. 5 shows how the density changes at $r = 2.6M$ for different values of b. As can be seen, for the non-rotating black hole, small values of b yield nearly identical results. It is observed that with increasing b, the density in the shock region increases slightly. At the same time, the opening angle of the shock cone also increases slightly. However, this increase is not as pronounced as in the rotating black hole case shown in Fig. 4. The cone curvature remains nearly symmetric around $\phi = 0$ for all values of b, because there is no frame dragging effect in this case.

In the right panel of Fig. 5, we compare the density variation at $r = 2.6M$ and $r = 6.08M$. At $r = 2.6M$, the density amplitude is larger and sharper compared to the situation at $r = 6.08M$. This indicates a stronger shock compression at $r = 2.6M$. Although increasing b slightly increases the density, this effect is much less significant than in the rotating black hole case. In other words, the effect of b is subtle compared to the rotating case. Due to the uniformity of the density around the non-rotating black hole, the resulting photon ring is also expected to be uniform. However, EHT observations have shown crescent brightness in the photon ring, which confirms that the observed black holes are rotating. In conclusion, the density behavior we find here is consistent with observational results.

4.4 QPOs from numerical data

Studying black holes using the BHL accretion mechanism, especially in strong gravitational fields, leads to the emergence of certain fundamental frequency modes. Moreover, due to the black hole rotation, additional physical effects arise via Lense–Thirring precession. Therefore, in such systems, studying QPOs not only helps theoretically reveal the impact of strong gravitational fields, but also provides a possible explanation for QPOs that have been observed but whose physical origin is not fully understood. When modeling the structure of the plasma that forms around the black hole through the BHL mechanism, the shock cone forms on the side opposite to the inflow direction, in what is called the downstream region [61,66,82,91–94]. Inside this cone, a stagnation point forms where the radial velocity of the falling matter becomes nearly zero. If matter lies between this point and the black hole horizon, it falls into the black hole. Otherwise, on the far side of the stagnation point, it would be carried away toward the computational boundary. The region between the stagnation point and the horizon behaves like a cavity that can trap oscillation modes. Therefore, both radial and azimuthal modes can be excited in this region, often resulting in the formation of LFQPOs. These modes typically emerge in three distinct forms. The first is the f_{EH} mode, which arises from the radial oscillation of matter between the stagnation point and the event horizon. This region acts as a resonant cavity, trapping pressure and velocity perturbations. The second is the f_{sh} mode, associated with oscillations occurring within the shock cone itself, especially in the radial direction. Finally, the f_{LT} mode results from the Lense–Thirring effect caused by the rotation of the black hole, leading to precession-induced modulations. Together, these modes contribute to the rich structure of QPOs observed in simulations of black hole accretion flows [82,92]. That is, the f_{sh}, f_{EH}, and f_{LT} modes can undergo nonlinear coupling, producing new peaks in the PSD analysis [99]. Together with these fundamental modes, the newly generated peaks can be used to explain the twin-peak HFQPOs observed in astrophysical systems. In other words, resonance conditions such as the $3:2$ ratio found in observations may be the result of these nonlinear couplings.

The dynamic structure of the shock cone, including its width and the location of the stagnation point, affects the characteristics of these modes. Additionally, variations in angular momentum also influence these oscillations. On the other hand, the angular momentum of matter orbiting in a strong gravitational field and the dynamics of the shock cone are modified by both the black hole spin parameter and the quantum correction term. Therefore, it is reasonable to expect that these parameters influence the observed QPOs. For all these reasons, we numerically demonstrate here the formation of QPOs occurring in strong gravitational fields around black holes.

In Fig. 6, the PSD analysis around the QCBH with varying b parameters is presented together with the Schwarzschild black hole case. As can be seen in each case of the PSD plot, a rich set of peaks is observed. The reason for this, as previously discussed, is that the fundamental peaks undergo nonlinear couplings, producing new peaks, and in some cases, these newly generated peaks themselves couple nonlinearly, either with the fundamental modes or with each other, to form additional peaks. In all cases, both LFQPOs and HFQPOs are detected. Furthermore, for $a/M = 0.0$, it is evident in every b case that above approximately 120 Hz, the peak amplitudes decrease and gradually approach the noise level. The noise amplitude is entirely dependent on the numerical method used, the numerical resolution, and other numerical artifacts, and thus can vary. For this reason, the detectability of frequencies above 120 Hz obtained from numerical simulations is quite low.

The detectability of LFQPO frequencies formed for different b values is significantly higher than in the Schwarzschild case. In the Schwarzschild case, the amplitude of the lowest-frequency peak is around 0.8 unit, whereas for different b values, it is about 1.6 units. This makes QPOs around QCBHs more likely to be observable. On the other hand, including the Schwarzschild case, the QPO frequencies (fundamentals and their nonlinear couplings) give rise to different resonance conditions. For example, in the $b = 0.1$ case, the ratios $21 : 13.8 \simeq 3 : 2$ and $37 : 25.3 \simeq 3 : 2$ appear, while at the same time ratios such as $21 : 7.4 \simeq 3 : 1$ and $51 : 25.3 \simeq 2 : 1$ also emerge. These ratios are characteristic of nonlinear coupling behavior and can be used to interpret the observed twin-peak HFQPOs in terms of fundamental diskoseismic or epicyclic modes [100,101].

Similarly, when comparing the QPO frequencies obtained for the Schwarzschild case and for $b = 0.2$, 0.4, 0.6, and 0.8, it is seen that the same resonance conditions occur as in the $b = 0.1$ case. Therefore, twin-peak resonance conditions such as the $3 : 2$ ratio observed with X-ray telescopes are more likely to be detected in QCBH systems compared to the Schwarzschild case. When the PSD analyses for different b values are compared in the non-rotating black hole case, it is observed that for $b = 0.6$, the LFQPOs, in particular,

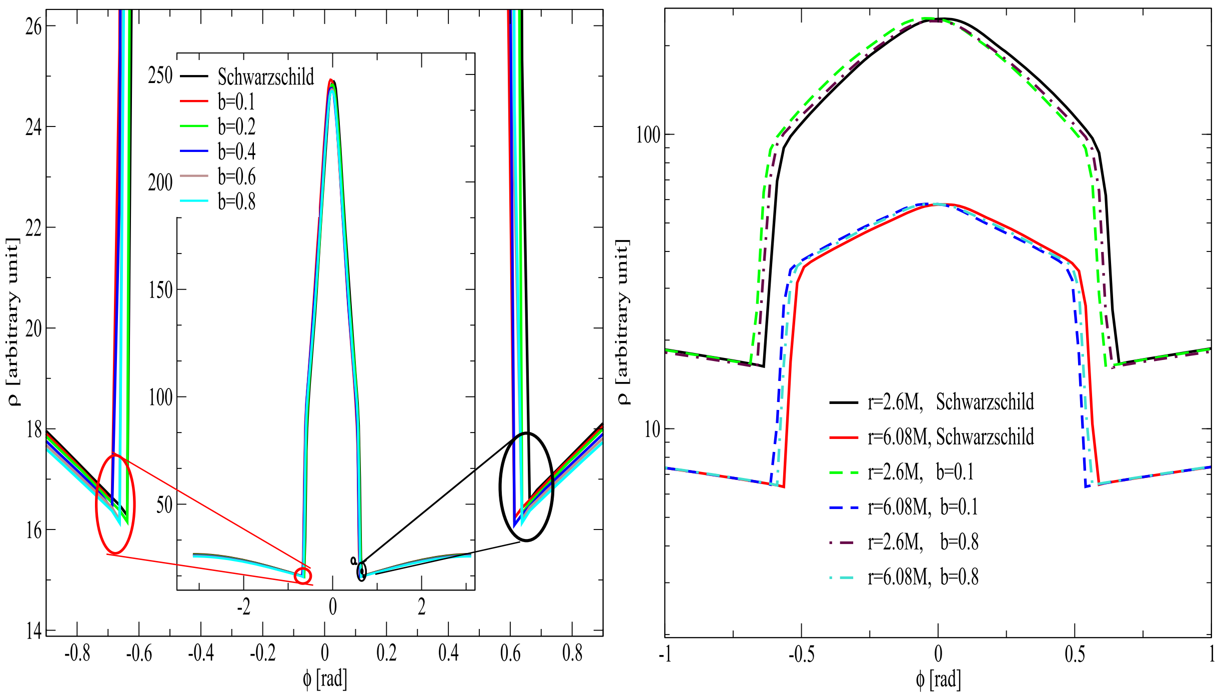

Fig. 5 It is the same as Fig. 4, but this time the spin parameter is $a/M = 0$, revealing the behavior around the non-rotating black hole. Since the black hole is non-rotating, no bending occurs in the shock cone as seen in Fig. 4. However, it is shown that the opening angle of the cone slightly changes with increasing b, compared to the Schwarzschild case

exhibit very high amplitudes, producing pronounced QPO peaks. Thus, we can state that $a/M = 0.0$ with $b = 0.6$ yields the most likely observable QPO frequencies for the non-rotating black hole model.

Finally, Fig. 6 shows three different PSD analyses with different colors. The first corresponds to the PSD calculated from the mass accretion rate dumped at the inner boundary of the computational domain ($r = 2.3M$), the second is the PSD calculated at $r = 6.08M$, very close to the ISCO, and the third is the PSD calculated from the mass accretion rate dumped at $r = 12M$, in a region where the gravitational field has weakened. It is observed that almost all QPO peaks occur at the same frequencies for all r values. This indicates that the modes are global oscillation modes. In other words, they are not caused by locally generated turbulence but are the result of global fundamental modes and their nonlinear couplings.

In Fig. 7, the PSD analysis for a moderately rotating black hole with $a/M = 0.5$ is carried out for both Kerr and QCBH cases with different values of b, revealing the QPO frequencies and the strength of their peaks. This analysis is performed at three radii: $r = 2.3M$ (in the strong gravitational field), $r = 6.08M$ (around the ISCO), and $r = 12M$ (a region where gravitational forces are relatively weak). In doing so, the radial and b-dependence of QPOs and the accretion-driven variability are investigated. As shown in Fig. 7, both LFQPOs and HFQPOs are observed around the moderately rotating black hole for Kerr and all QCBH cases. The frequency values of the PSD peaks calculated at different radial points are almost identical, which, as discussed previously for the $a/M = 0$ case, indicates that these oscillation modes are global rather than arising from local instabilities. When examining the PSD analyses for Kerr and QCBH at each b value, it is seen that the most dominant peaks occur around ~ 22 Hz at $r = 6.08M$, i.e., near the ISCO. This suggests that in the moderately rotating black hole model, the likelihood of observing the strongest peaks is highest near the ISCO.

As in the $a/M = 0$ case, various observable resonance conditions are produced for $a/M = 0.5$. For example, in the $b = 0.2$ case, the ratios $22.8 : 15 \simeq 3 : 2$, $27 : 18.4 \simeq 3 : 2$, and $33 : 22.8 \simeq 3 : 2$ correspond to twin-peak harmonic resonances, while other ratios such as $58 : 27 \simeq 2 : 1$, $22.8 : 10.5 \simeq 2 : 1$ and $33 : 10.5 \simeq 3 : 1$ also emerge, which are considered possible for different astrophysical sources. Similarly, when the peaks for different b values of Kerr and QCBH are analyzed, these resonance conditions are also found. Again, such ratios $3 : 2$, $2 : 1$, $3 : 1$ etc. are the result of nonlinear mode couplings. The strong HFQPOs with these resonance relationships are exactly the kind of patterns seen in X-ray observations of twin-peak HFQPOs in black hole binaries.

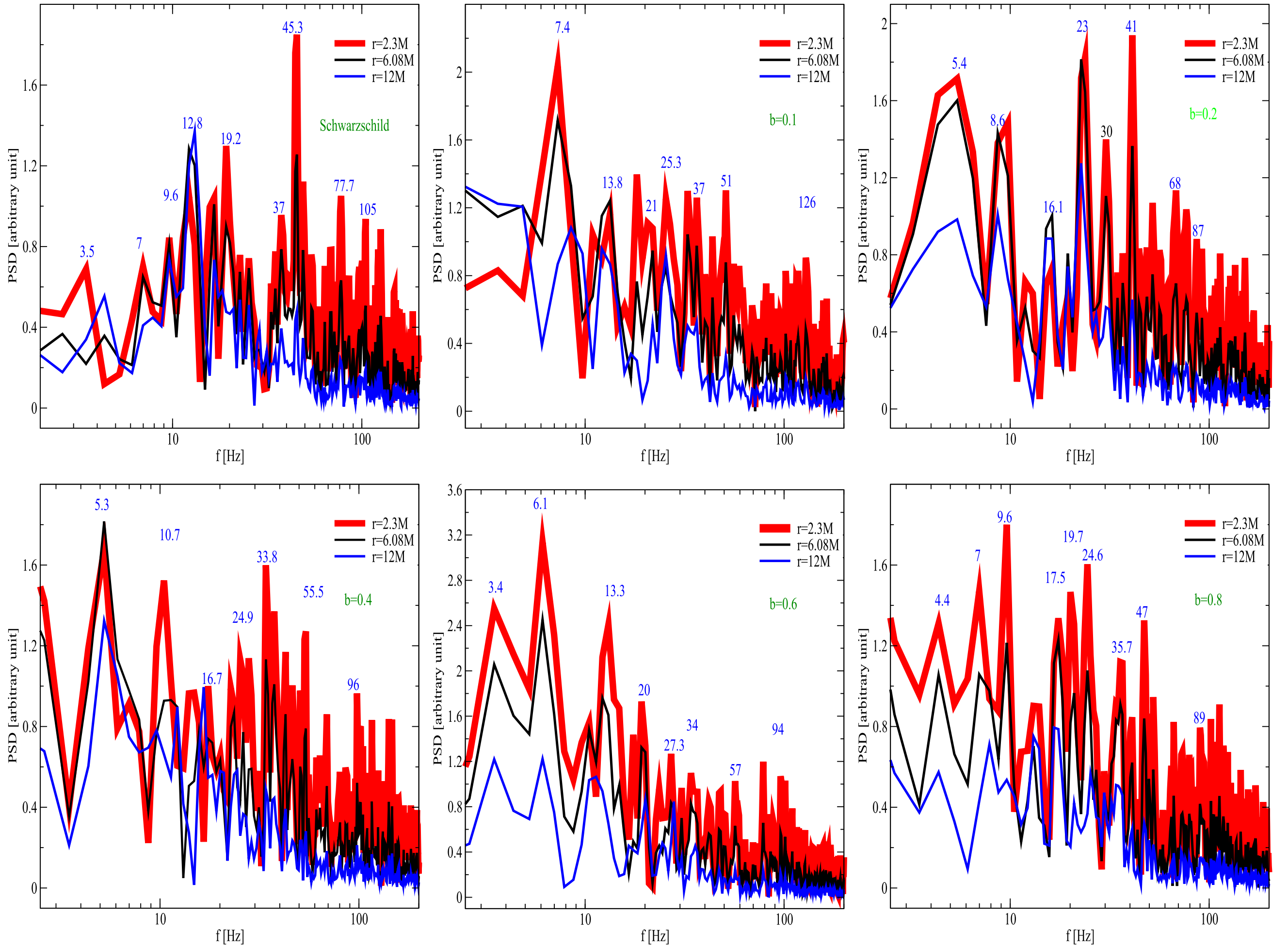

Fig. 6 In the case of a non-rotating black hole with $a/M = 0$, the variation of the PSD peaks obtained from the mass accretion rate calculated at different locations has been shown as a function of frequency for $M = 10M_{\odot}$. While LFQPOs are observed in each case, it is found that the peaks around the QCBH and their corresponding frequencies are not significantly different from those of the Schwarzschild black hole

When comparing the Schwarzschild case in Fig. 6 with the Kerr case in Fig. 7, LFQPOs are found to be more observable in the Kerr case. This is consistent with theory, as it is theoretically known that LFQPOs arise in strong gravitational fields due to the Lense–Thirring effect. As discussed previously for Fig. 6, such LFQPOs are also excited in QCBH cases. Therefore, when comparing the QCBH cases in Fig. 6 with the Kerr and QCBH cases in Fig. 7, we can conclude that LFQPOs are observable in all these situations. This suggests that QPO frequencies generated around QCBHs can be produced at amplitudes high enough to be detected in strong gravitational fields.

As in Fig. 6, because the amplitudes of frequencies above $\sim$ 120 Hz are very small, it is very difficult to determine whether they are physical or not due to numerical simulation errors. However, the LFQPOs and HFQPOs that occur at lower frequencies are the result of fundamental modes and their couplings, and their amplitudes are well above the noise level. In conclusion, the PSD analysis shows that both LFQPOs and HFQPOs are generated around the moderately rotating black hole. Although b generally does not significantly change QPO frequencies, it can suppress or enhance peak strengths. Nevertheless, regardless of b, the strong gravitational field remains the most active region for QPO observations. At a spin value of $a/M = 0.5$, the moderate frame-dragging effect can support mode trapping and coherent motion.

According to the PSD analysis in Fig. 8, the peaks formed at $r = 2.3M$ appear to be suppressed by approximately a factor of 15–20 compared to those at other radial locations. This may possibly be due to the effect of frame dragging caused by high spin near the horizon. On the other hand, clear and strong peaks are observed around the ISCO, at $r = 6.08M$. These peaks appear as both LFQPOs and HFQPOs.

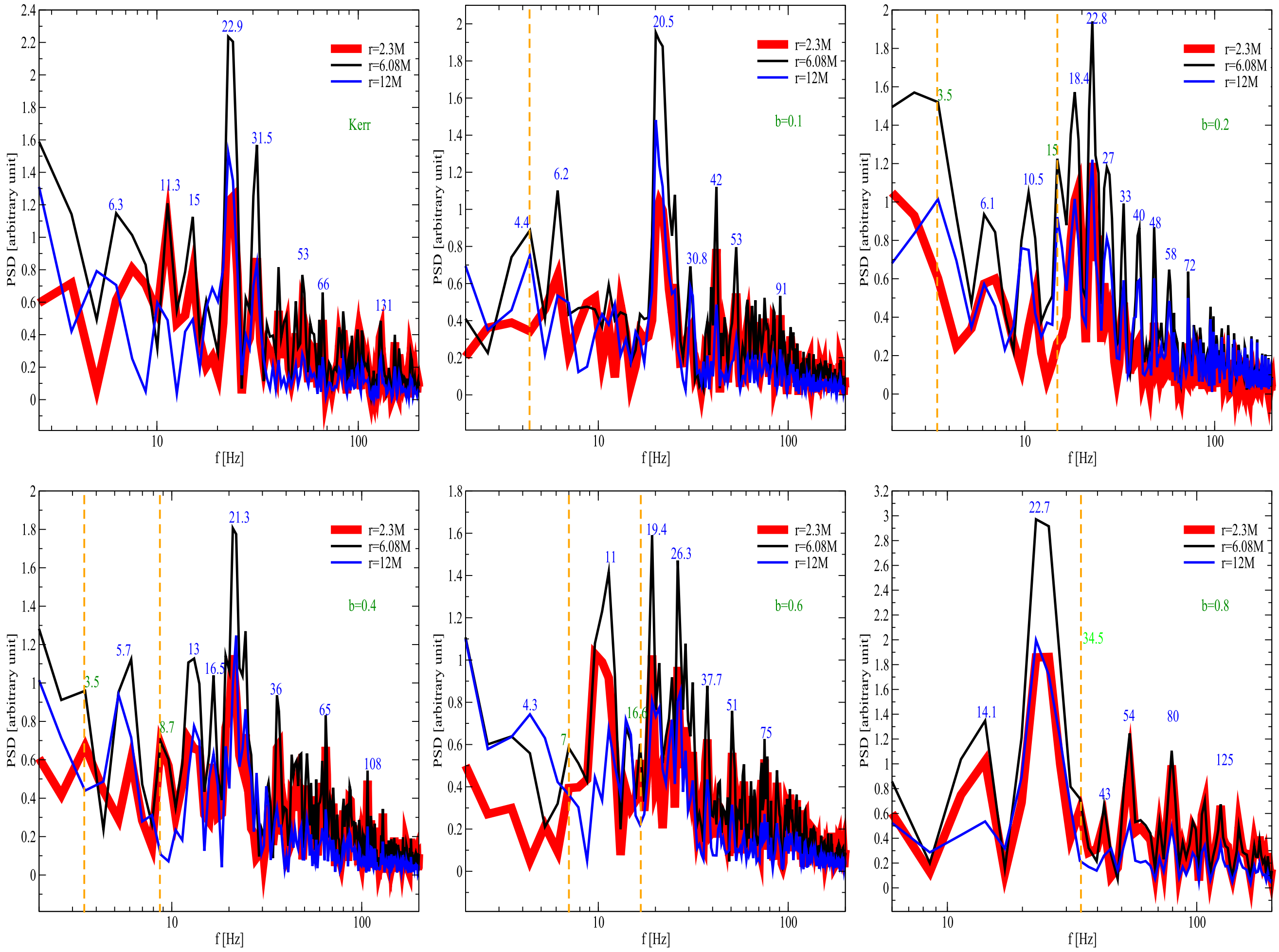

Fig. 7 In the case of a rotating black hole with $a/M = 0.5$, the variation of the PSD peaks obtained from the mass accretion rate calculated at different locations has been shown as a function of frequency for $M = 10M_{\odot}$. While LFQPOs are observed in each case, it is found that the peaks around the QCBH and their corresponding frequencies are not significantly different from those of the Kerr black hole

In particular, the peaks formed in the 11–15 Hz range become more prominent in the rapidly spinning black hole model, likely due to the shock cone and its instabilities. Although the peaks at $r = 12M$ are weaker than those at $r = 6.08M$, they are still strong enough to be observable. These results indicate that in high-spin black hole models, the region where QPOs form tends to shift outward and cover a wider area. The influence of the parameter b on QPOs around QCBHs is also evident. For nearly all values of b, the frequencies lie within the 3–15 Hz range. At high values of b, such as $b = 0.6$ and $b = 0.8$, the peaks tend to broaden or become dampened. This may be due to an increase in turbulence intensity, modified shock geometry, and the smoothing of small-scale structures by spacetime curvature. These results are consistent with previous Figs. 6 and 7 and support the idea that QCBHs retain essential observational signatures such as QPOs, even under quantum modifications.

As in Fig. 7, it is clearly seen in Fig. 8 that LFQPOs are excited due to the Lense–Thirring effect. In addition, when compared with Figs. 6 and 7, it is observed that the maximum HFQPO frequency, which occurs around ~ 120 Hz in those cases, appears around ~ 80 Hz for $a/M = 0.9$. This indicates that the spin parameter suppresses HFQPOs while exciting LFQPOs [102]. Therefore, according to the PSD analyses for $a/M = 0.9$, the detectability of frequencies above ~ 80 Hz may be limited due to numerical difficulties and artifacts. As in the $a/M = 0$ and $a/M = 0.5$ cases, a rich set of QPO peaks is produced as a result of the fundamental modes and their nonlinear couplings. When the frequencies corresponding to these peaks are analyzed, it is again found that resonance conditions known from both observations and theory are present. For example, in the case of $a/M = 0.9$ and $b = 0.2$, ratios such as $17.4 : 8.6 \simeq 2 : 1$ and $8.6 : 5.2 \simeq 3 : 2$ are observed.

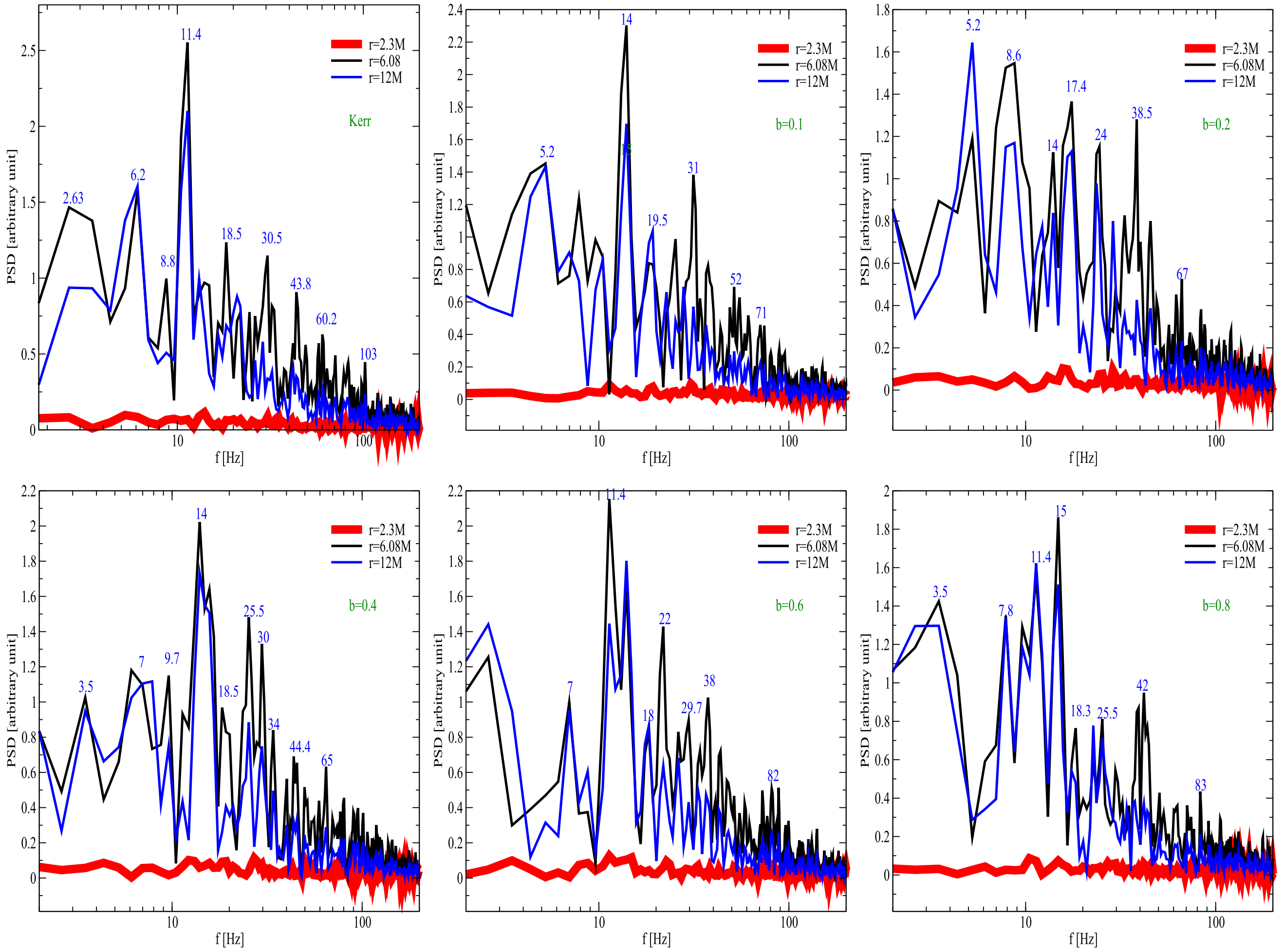

Fig. 8 In the case of a rapidly rotating black hole with $a/M = 0.9$, the variation of the PSD peaks obtained from the mass accretion rate calculated at different locations is shown as a function of frequency for $M = 10M_{\odot}$. While LFQPOs are observed in each case, it is found that the peaks around the QCBH and their corresponding frequencies are not significantly different from those of the Kerr black hole. However, the amplitude of the peak at $r = 2.3M$ is about 15 times smaller than those at other radial locations, indicating that their observability is considerably reduced

4.5 Applicability of shock cone QPO mechanism to supermassive black holes and AGNs

Although in this work we focus on identifying the oscillation modes trapped inside the shock cone produced by BHL accretion around QCBHs and the resulting QPO frequencies, it is equally important to discuss and ultimately to establish the applicability of these results to different astrophysical environments. Our numerical models, which correspond to low-angular-momentum inflows that form shock cones known, directly reproduce the QPO behavior observed around stellar-mass black holes in XRBs. As explained in detail above, the fundamental oscillation modes identified in our simulations are f_{sh}, f_{EH}, and f_{LT}.

A key outcome of our numerical simulations is that both the shock cone structure and the excited QPO frequencies are fundamentally scale-invariant. Throughout this paper we have used geometrized units, where the frequency has dimensions of $1/M$. This immediately implies that the same physical mechanism can, in principle, be extended to supermassive black holes and AGNs, once the frequencies are rescaled with black hole mass. To carry out this conversion, we use the relation $\nu(Hz) = \frac{c^3}{GM_{BH}}\nu_{geo}$. Where ν_{geo} is the frequency in geometrized units computed in numerical simulations and M_{BH} is the black hole mass. Application of this scaling shows that frequencies in the tens-hundreds of Hz range for stellar-mass systems shift naturally into the microhertz-millihertz regime for supermassive black holes. The robustness of the shock cone mechanism therefore implies that QPO generation does not exclusively require thin disk physics, but can emerge from the hydrodynamic response of matter to strong gravity.

On the other hand, traditional diskoseismology models (p-, g-, and c-modes) face challenges when applied to AGNs, even though they are often successful in describing QPOs in XRBs [103]. Moreover, a recent study by [104] emphasizes that the detectability of HFQPOs in AGNs depends not only on black hole mass but also sensitively on the accretion state, which governs whether oscillations can be trapped and excited. Our results complement these findings by demonstrating that consistent QPO modes can also arise from shock-cone dynamics, providing an additional and independent physical pathway to variability. The motivation for extending this model to AGNs is strongly reinforced by recent EHT observations of $M87*$ [91] and $SgrA*$ [79,82], which place constraints on accretion morphology, variability, and horizon-scale dynamics. In particular, time-domain analyses of horizon-scale images may be able to test whether oscillatory features consistent with shock cone QPOs are present in AGN. Bridging the shock-driven QPO framework developed here with these large-scale observational efforts represents a natural continuation of this work.

It is important to acknowledge that the present simulations neglect certain features of realistic AGN accretion flows, including high angular momentum thin disks, strong radiative feedback, magnetic fields, and turbulence in the vertical direction. These factors may influence the detailed morphology of the accretion flow, the amplitudes of oscillation modes, and their coherence. Nevertheless, the existence of a hydrodynamic cavity capable of trapping perturbations is a generic and physically motivated feature of curved spacetime accretion flows. Thus, the shock cone mechanism identified here is not an artifact of simplifying assumptions.

In conclusion, although the results presented here are directly applicable to XRBs, the underlying physical mechanism and the resulting QPOs can be rescaled with black hole mass and extended to AGNs. Demonstrating this applicability not only tests the reliability and universality of the shock cone mechanism but also provides a complementary approach to traditional QPO models. This opens the door to new interpretations of variability in both X-ray data and horizon-scale observations. Indeed, in our earlier studies using different modified gravity theories, we also found that the shock cone mechanism could operate in both stellar-mass and supermassive black hole systems, with numerical results consistent with observed QPOs in AGN [105].

4.6 Parameter space analysis

Revealing the behavior of matter around a QCBH, the dynamic structure of the resulting shock cone, and the effect of pressure forces on spacetime curvature in a strong gravitational field is crucial for determining the behavior of numerically computed QPOs. At the same time, understanding this behavior is also important for revealing how QCBH affects Kerr spacetime. Therefore, in each model scenario, we calculate a complexity indicator based on the number of time steps required up to $t_{max} = 40,000M$. This indicator quantifies the intensity of the interaction occurring around the black hole. The complexity indicator $\mathcal{N}(b)$ is given as

$$\mathcal{N}(b) = \frac{T_b - T_{\text{Kerr}}}{T_{\text{Kerr}}}. \tag{4.3}$$

Here, T_b represents the total number of time steps in the presence of a given quantum correction parameter b, while Kerr is the number of time steps in the standard Kerr black hole scenario.

Figure 9 shows how this factor changes for a spin parameter $a/M = 0.9$. It demonstrates how the accreting dynamics of infalling matter are affected by the parameter b in the QCBH geometry. The complexity indicator decreases monotonically, indicating that the required number of time steps decreases as b increases. Figure 3, again for the case $a/M = 0.9$, illustrates how the mass accretion rate evolves over time after the shock cone reaches the steady state at the inner boundary of the computational domain, at $r = 2.3M$. This figure strongly supports why the complexity indicator decreases with increasing b. As seen in the figure, while in the Kerr case a high oscillation amplitude and erratic accretion rate are observed, the amplitude steadily decreases with increasing b. This shows that the quantum correction parameter suppresses dynamic instability and turbulence.

The results obtained from the numerical calculations agree well with the analytical results based on the motion of the test particle [36]. The numerical results also indicate that the spacetime curvature effects induced by the black hole spin parameter may be partially suppressed. In fact, the quantum correction term added to the Kerr metric regularizes the black hole geometry, suppresses curvature singularities, and weakens gravitational attraction.

The quantum correction term b plays a significant role in strong gravitational fields or in regions near the horizon. This is illustrated in Fig. 10. In Fig. 10, the variation of the time-averaged normalized mass accretion rate with respect to b is shown at different radial positions long after the disk has reached the steady state around the Schwarzschild black holes, moderately rotating and rapidly rotating. Normalization is obtained by dividing the mass accretion rate at each value of b by its value at $b = 0$. As can be seen in Fig. 10, in the strong gravitational field ($\sim$ 2–3), the mass accretion rate increases with increasing b. On the other hand, at $r = 6.08M$ and $r = 12.03M$, this variation with respect to b is minimal. As also shown in theoretical studies [36], in strong gravitational fields, the quantum correction term modifies the g_{tt} and g_{rr} components of the spacetime metric. Therefore, the parameter b affects the effective potential, the infall velocity of matter, the accreted mass, and thus the accretion rate.

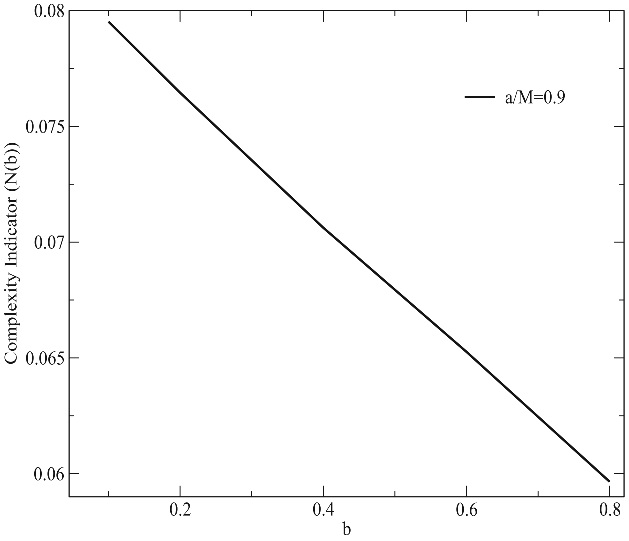

Fig. 9 Complexity indicator

Moreover, since the quantum correction term decreases as b^2/r^2, its influence becomes negligible or comparable to the Kerr geometry at $r \geq 6M$. Additionally, when comparing the change in the accretion rates under different spin parameters with those in Kerr geometry, it is clearly observed that for the rapidly rotating black hole, the mass accretion variation due to b in the strong gravity region is more pronounced in the case of $a/M = 0.9$ compared to $a/M = 0.5$ and $a/M = 0.0$. This demonstrates that the frame-dragging effect caused by the high spin of the black hole, along with redshift phenomena, significantly influences the mass accretion rate. In other words, in this strong gravitational region, matter approaching the horizon rotates faster and becomes denser.

As a result, the modifications introduced by the quantum correction term in strong gravitational fields may manifest as observable features in high-energy astrophysical phenomena. This reveals a potentially significant and distinguishable physical effect in EHT observations [106–108] and $X-$ray spectrometry [109].

In Figs. 3 and 10, the variation of the mass accretion rate with respect to a/M and b is investigated. While the accretion rate (given in arbitrary units) increases significantly as a/M increases, this behavior has been observed to not change much with variations in b. The parameter b only significantly alters the mass accretion rate in the case of a rapidly rotating black hole with $a = 0.9$ at $r = 2.3M$, as seen in Fig. 10, within the strong gravitational field. It is clearly shown that as b increases, the mass accretion rate also increases. In addition, for a moderately rotating black hole with $a/M = 0.5$, again at $r = 2.3M$, it is observed that the mass accretion rate only shows a slight difference. On the other hand, for all values of a and r, the oscillation of the mass accretion rate around a certain value decreases as b increases.

These changes evidently have a significant impact on observations such as black hole shadows, gravitational waves, and QPOs in the strong gravitational fields, and they imply a clear deviation when compared to the Kerr black holes. While the spin of the black hole increases turbulence around it due to the frame-dragging effect, the quantum correction acts like a damping mechanism. As a result, it suppresses high-frequency fluctuations and regularizes the geometry, especially close to the horizon.

The combined effects of a/M and b on the accretion rate and thus on the disk structure can be seen in the top-left snapshot of Fig. 3 and the left snapshot of Fig. 10. This shows that b plays a critical role when the black hole has a rapid rotation parameter a/M, particularly in the strong gravitational field near the horizon (e.g., at $r = 2.3M$). It dampens turbulence, reduces chaotic accretion fluctuations, and stabilizes

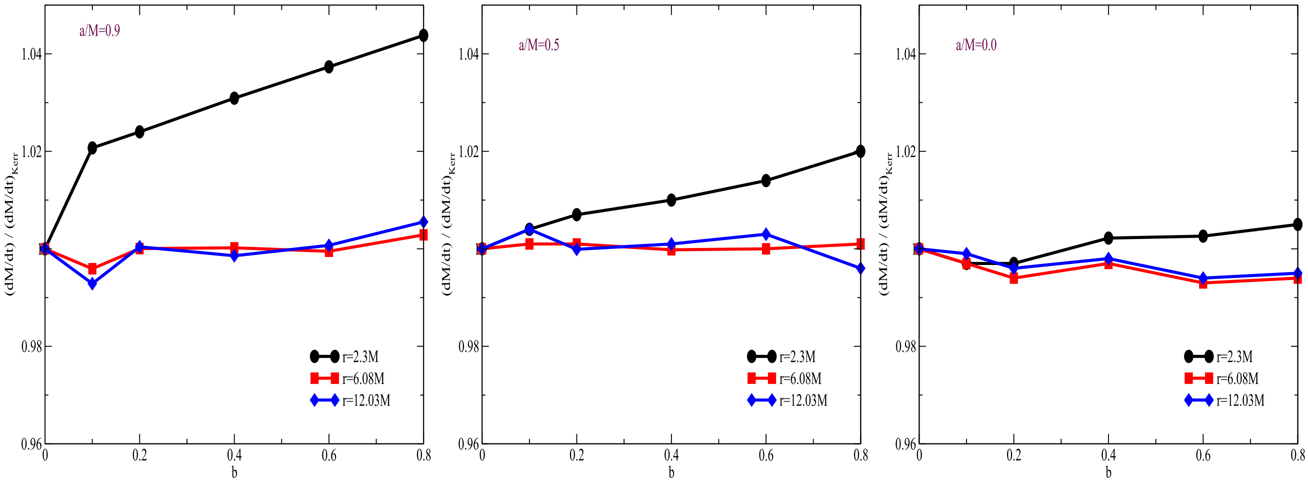

Fig. 10 The variation of the normalized mass accretion rates with respect to b is shown, normalized by the Kerr mass accretion rate for the various values of a/M. It is clearly seen that the parameter b influences the amount of matter falling toward to the black hole

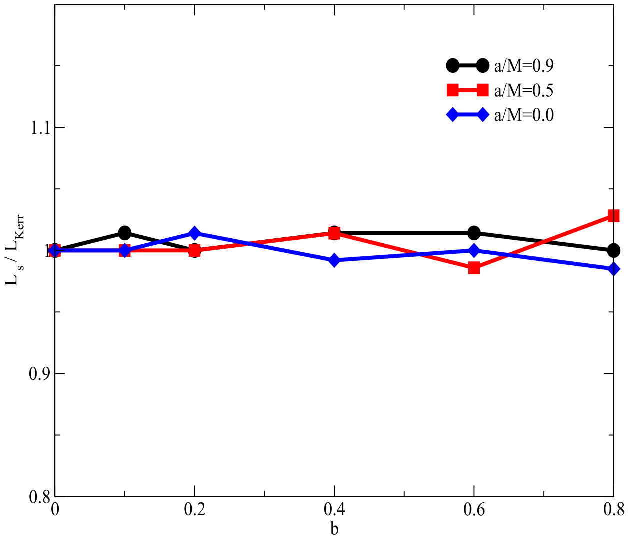

Fig. 11 The variation of the stagnation point formed inside the shock cone around the black hole for various spin parameter is shown with respect to the quantum correction term b. It is observed that the location of the stagnation point remains nearly the same as b varies

the dynamics of the shock cone, highlighting its observable impact in simulations and potential detectability via X-ray or EHT data.

The important physical results that we have numerically revealed around QCBHs, which are potentially distinguishable by observation, are consistent with existing studies in the literature. For example, [36] analytically demonstrated that b changes QPO frequencies by changing the ISCO. These results are in direct agreement with our numerical findings. Furthermore, the finding that quantum corrections lower QPO frequencies and slow down dynamics [39,110] is consistent with our observation that QPOs are damped and the mass inflow becomes smoother as b increases. Similarly, as found by [111], the infall structure near quantum-inspired horizons is also suppressed, supporting our numerical results. In addition, [22] has shown that regularizing the singularity and horizon leads to different dynamical properties, such as reduced ringdown frequencies, further supporting the findings presented in this study.

In Fig. 11, the variation of the stagnation point – normalized with respect to the Kerr solution – is shown as a function of the quantum correction parameter b for different values of the spin parameter a/M. The stagnation point represents the location inside the shock cone where the radial component of the accretion flow becomes zero. The matter trapped between the black hole and the stagnation point eventually is accreted toward the black hole. As seen in Fig. 11, the ratio $L_s/L_{\rm Kerr}$ is approximately equal to 1 for all values of b, regardless of the spin a/M. This indicates that the parameter b has a minimal effect on the location of the stagnation point. Consequently, the structure of the shock cone remains nearly unchanged with varying b.

According to previous studies and theoretical models, QPOs originate near the black hole and often within the shock cone. The constancy of the stagnation point suggests that the formation region of QPOs does not change significantly with b, which is why the QPO frequencies remain mostly unaffected. This outcome is consistent with the PSD analyzes shown in Figs. 6, 7, and 8. Therefore, the QPOs observed around QCBHs exhibit robust behavior for $b \in [0.1, 0.8]$. On the other hand, the morphology of the black hole shadow also does not vary significantly with b. This implies that the shadow structure around a QCBH resembles that of a Kerr black hole. These results are consistent with the EHT observations of $M87^*$ and $Sgr A^*$, where the observed shadows do not deviate significantly from the Kerr predictions. Finally, the variation of the spin parameter a/M does not considerably affect the stagnation point either. This suggests that b does not interact strongly with spin to alter the stagnation zone.

5 Accretion dynamics in the absence of an event horizon

Naked singularities are hypothetical astrophysical objects that lack an event horizon and therefore may be distinguishable from black holes through observational data. Due to the high energy and luminosity of their surrounding accretion disks, naked singularities can be differentiated from Kerr black holes [112,113]. Reflective naked singularities produce distinctive bright rings in the central regions of their accretion disk images. While these features may not be detectable with the current EHT, they could potentially be observed using the next-generation high-frequency EHT instruments [114]. Additionally, naked singularities may be identified by analyzing frequency shifts observed in redshift data from various sources [115]. Although they have not been observed yet due to the limitations of current observational technologies, advancements in telescope sensitivity and new instruments may enable us to understand the physical characteristics of these exotic objects.

In the case where the black hole spin parameter is $a/M = 0.9$, as shown in Figs. 2, 3, 4, 8, 10, and 11, if $b > 0.22$, no event horizon forms, and the spacetime contains a naked singularity. This indicates that a classical black hole does not form. This also shows that when $b > 0.22$, the quantum correction becomes strong enough to prevent the formation of a horizon, resulting in the emergence of only a naked singularity.

Nevertheless, even in the presence of a naked singularity, we can still model the plasma structures that arise via the BHL accretion mechanism. As seen in Fig. 2 for the case $a/M = 0.9$ and $b = 0.4$, a shock cone still forms, and its dynamic structure does not differ significantly from the case with $b = 0$. Furthermore, as observed in the graph on the left of the first row in Fig. 3, the accretion rate increases with increasing b. This behavior appears to be independent of whether the object is a classical black hole ($b < 0.22$) or not ($b > 0.22$).

Indeed, since in our numerical simulations the inner boundary of the computational domain is fixed at $r = 2.3M$, and since the quantum correction term affects the spacetime equally regardless of whether the black hole or naked singularity is present, it has been observed in Figs. 2, 3, 4, 8, 10, and 11 that the shock cone formed around the object and hence the resulting QPOs are not significantly affected by whether the object is the black hole or a naked singularity.

Moreover, since the numerical simulations around the naked singularity employ the same outflow boundary condition as those around the black holes, they are not only physically valid but also scientifically interesting. This is because they allow us to test strong-field region in regimes beyond standard black holes. Additionally, modeling the plasma structure around the naked singularity may enable tests of the cosmic censorship conjecture, and may also offer potential explanations for anomalous observational features observed in black hole shadow or QPO data.

6 Discussion and conclusions

In this paper, we thoroughly discuss how the accretion dynamics around QCBHs, resulting from BHL accretion, and the structure of the resulting shock cone change depending on the parameters a/M and b. We reveal how the accretion mechanism is influenced by these parameters and examine in detail the interplay between the black hole spin parameter a/M and the quantum correction parameter b, along with its consequences. By analyzing this interaction in the strong gravity region near the ISCO, as well as in regions with weaker gravitational fields, we identify the QPO modes trapped inside the shock cone. The structure of the shock cone and the resulting QPOs around QCBHs are compared with those obtained in the classical Kerr case, showing that the inclusion of the quantum correction parameter b introduces distinct and measurable modifications to both the accretion flow and the resulting QPO spectra.

It has been observed that the mass accretion rate obtained from BHL accretion, where matter falls into the black hole, is strongly dependent on both a/M and b. As expected, a change in the radial position also causes a change in the accretion rate. Theoretically, it is known that the black hole spin parameter and b affect the accretion dynamics. Therefore, the results we find here agree with the theoretical predictions. In particular, for the rapidly rotating black hole case, significant changes in the mass accretion rate are observed at $r = 2.3M$ with increasing b. The systematically increasing mass accretion rate with increasing b shows that the quantum correction modifies the gravitational field and facilitates matter inflow. Compared to the Kerr case, this effect is found to be more pronounced in the QCBH case. These findings are also well-founded in theoretical models [36,116].

On the other hand, as the distance from the black hole increases, it is observed that the accretion rate oscillates around a certain value for different b values, and the behavior becomes more unstable and turbulent. This reveals that the strong frame-dragging effect stabilizes accretion, while around the ISCO region, shock wave interactions become more dominant. In the case of a moderately rotating black hole, it can be said that b significantly affects accretion in the strong gravitational field, while it has almost no effect in the outer regions. These results show that b is not very effective in weakly relativistic regions or for slowly or non-rotating black holes. In conclusion, it has been seen that both a/M and b modify spacetime in strong gravitational fields and alter the dynamics of accretion. Therefore, these changes significantly affect the photon spheres of $M87^*$ and $SgrA^*$, as observed by the EHT.

The emergence of QPOs around the classical and quantum-corrected black holes is crucial for revealing the properties of both the black hole and the surrounding plasma. Through QPO analysis, the oscillation modes and their origins can be determined as a function of spin parameter a/M and quantum correction parameter b, allowing us to test the nature of strong gravitational fields around QCBHs compared to Kerr black holes. The numerical results summarized in Table 2 show that both a/M and b significantly affect the formation, location, nature, and strength of QPOs. In the case of a rapidly rotating black hole with $a/M = 0.9$, it is found that strong frame dragging stabilizes oscillations near the horizon, leading to dominant QPO peaks at $r = 6.08M$. The QPO frequencies range between 3–25 Hz for LFQPOs and 25–131 Hz for HFQPOs. Although b does not alter the QPO frequencies, it modifies the peak amplitudes that determine their observability. These results are consistent with XRB observations of type-C LFQPOs, where stronger spin often correlates with more coherent oscillations at higher frequencies [117,118].

In the case of a mildly rotating black hole with $a/M = 0.5$, both coherent motion and QPO trapping are observed. Numerical calculations show LFQPOs in the range 5–10 Hz and HFQPOs in the range 20–23 Hz. Additionally, b influences the amplitude of the observed peaks. These results are compatible with observations from the source GRS 1915+105 [119,120], where multiple peaks have been reported and the spin is known to be intermediate.

In the non-rotating case ($a/M = 0.0$), where frame dragging is absent and symmetric oscillations dominate, the largest amplitude peaks appear at $r = 2.3M$. QPO frequen-

Table 2 Comparison of QPOs based on black bole spins are given below

Feature	$a/M = 0.9$	$a/M = 0.5$	$a/M = 0.0$
QPO frequency range	LFQPOs: 3–25 Hz HFQPOs: 25–103 Hz	LFQPOs: 5–25 Hz HFQPOs: 25–131 Hz	LFQPOs: 4–25 Hz HFQPOs: broad shoulder above 30 Hz (only at $r = 2.3M$)
Dominant radius	$r = 6.08M$: dominant peaks $r = 2.3M$: almost flat PSD	$r = 6.08M$: strongest QPOs $r = 2.3M$: strong LFQPOs	$r = 2.3M$: sharpest peaks $r = 12M$: weakest
Effect of b	QPO freq. stable with b Peak modulated by b	Freq. similar to Kerr Enhanc.-suppress. peaks with b	Very small effect on QPO Slight modulation
Frame dragging effect	Strong – stabilizes inner region Shifts variability outward	Moderate – allows trapping and coherent motion	Absent – symmetric oscillations
PSD at $r = 2.3M$	Flat or suppressed power	Noticeable peaks	Strong LFQPOs
Reasons of peaks	Fundamental modes and Nonlinear couplings	Fundamental modes and Nonlinear couplings	Fundamental modes and Nonlinear couplings

cies are highly stable (LFQPO: 4–13 Hz), with an additional broad HFQPO shoulder above 40 Hz observed only in the inner radius, which is mainly seen in some XRB systems (e.g., GRO J1655-40) [121]. The effect of b in this case is minimal. This scenario is consistent with observations of low-luminosity AGNs, where LFQPOs are more common and the oscillations are concentrated around the ISCO [104].

From the PSD analyses, it has been shown that the fundamental oscillation modes f_{sh}, f_{EH}, and f_{LT} become trapped within the shock cone, giving rise to both LFQPOs and HFQPOs. Importantly, nonlinear couplings among these modes produce resonance conditions such as the characteristic $3:2$ ratio, consistent with X-ray observations of black hole binaries. The numerical results further indicate that, with increasing b, high-frequency peaks near the horizon are suppressed, the QPO-generating region becomes broadened, and the mode amplitudes are modified. Thus, the peaks formed around QCBHs provide a distinctive observational fingerprint.

In models with high mass accretion rates and strong oscillations or turbulence, it is also plausible that QPO behavior influences the black hole shadow observed by EHT. A shock cone located very close to the horizon, coupled with strong oscillations, can significantly affect the brightness of the photon ring. Frame dragging produces crescent-like emission features, which are observed in simulations of rapidly rotating black holes. This aligns with the asymmetric brightness observed in the EHT images of $M87^*$ and $SgrA^*$ [5–9]. The numerical results also show that the parameter b does not drastically alter the formation of QPOs or the dynamics of accretion. This implies that quantum corrections do not erase the key observational signatures detectable by instruments such as EHT or NICER [122].

Extending the analysis to astrophysical systems, we discussed that QPOs excited by the shock cone mechanism can be applied not only to XRBs but also to systems hosting supermassive black holes at their centers, as well as to AGNs. At the same time, the emergence of resonance conditions across different parameters indicates that QPOs can serve as a unifying diagnostic tool across mass scales, bridging microquasars and AGNs. On the other hand, we also discussed the physical phenomena obtained around the naked singularity. Although the resulting frequencies and amplitudes are modified, the formation of a shock cone and the emergence of QPOs are still observed in the naked singularity scenario. This suggests that, with increasing sensitivity of telescopes, it may become possible to observe theoretically predicted naked singularities.

Numerical simulations have shown that the location of the stagnation point changes very little with respect to a/M and b. This indicates that the accretion flow formed around the QCBHs is highly robust. The fact that the stagnation point remains nearly the same across all parameters supports the observational consistency between QCBHs and classical Kerr predictions. In fact, current high-resolution observations-such as those from the EHT-have not detected any significant deviation from the Kerr model. Therefore, the shadow structure observed by the EHT also supports the QCBH model [5–9].

As a result, although the mass accretion ratios calculated around QCBHs and Kerr black holes can be distinguishable in the strong gravitational fields near rapidly rotating black holes as seen in Fig. 10, the QPO frequencies generated around these black holes are in close agreement, with only very slight modifications. Therefore, it is highly challenging to determine which type of black hole the observed QPOs originate from. This outcome is consistent with the study conducted in [54,110] regarding black hole shadows.

Finally, numerical simulations have shown that, depending on the quantum correction parameter, whether the classical black hole forms or not, in both cases the plasma structure, shock cone, and QPO modes developing around the black hole or naked singularity exhibit similar behavior. We believe this could help explain certain observational data from the EHT and X-ray observations that cannot be accounted for by assuming a purely classical black hole. Therefore, we consider the numerically obtained results in the naked singularity case to be scientifically valuable and a meaningful contribution to the literature. The results presented here also suggest that the calculated QPOs may open a new window for testing quantum gravity in the strong gravitational regime. In the future, with increasingly sensitive observations from telescopes such as the EHT and X-ray missions, it will be possible to constrain the parameter space of QCBHs and distinguish them from classical black holes.

Acknowledgements All simulations were performed using the Phoenix High Performance Computing facility at the American University of the Middle East (AUM), Kuwait. I would like to express my gratitude to the referee for their contributions aimed at enhancing the quality of the manuscript.

Data Availability Statement Data will be made available on reasonable request. [Authors' comment: The datasets generated during and/or analysed during the current study are available from the corresponding author on reasonable request.]

Code Availability Statement Code/software cannot be made available for reasons disclosed in the code availability statement. [Authors' comment: The code generated during and/or analysed during the current study is not publicly available due to its non-user-friendly structure and lack of sufficient documentation for external use.]

Funded by SCOAP^3.

References

1. J.R. Oppenheimer, H. Snyder, On continued gravitational contraction. Phys. Rev. **56**, 455–459 (1939)
2. R. Abbott, T.D. Abbott, S. Abraham, F. Acernese, K. Ackley, A. Adams et al., Search for lensing signatures in the gravitational-wave observations from the first half of LIGO-Virgo's third observing run. APJ **923**, 14 (2021). arXiv:2105.06384
3. R.P. Kerr, Gravitational field of a spinning mass as an example of algebraically special metrics. Phys. Rev. Lett. **11**, 237–238 (1963)
4. B.P. Abbott, R. Abbott, T.D. Abbott, M.R. Abernathy, F. Acernese, K. Ackley et al., Observation of gravitational waves from a binary black hole merger. PRL **116**, 061102 (2016). arXiv:1602.03837
5. Event Horizon Telescope Collaboration, K. Akiyama, A. Alberdi, W. Alef, K. Asada, R. Azulay et al., First M87 event horizon telescope results. I. The shadow of the supermassive black hole. APJl **875**, L1 (2019). arXiv:1906.11238
6. Event Horizon Telescope Collaboration, K. Akiyama, A. Alberdi, W. Alef, K. Asada, R. Azulay et al., First M87 event horizon telescope results. II. Array and instrumentation. APJl **875**, L2 (2019). arXiv:1906.11239
7. Event Horizon Telescope Collaboration, K. Akiyama, A. Alberdi, W. Alef, K. Asada, R. Azulay et al., First M87 event horizon telescope results. III. Data processing and calibration. APJl **875**, L3 (2019). arXiv:1906.11240
8. Event Horizon Telescope Collaboration, K. Akiyama, A. Alberdi, W. Alef, K. Asada, R. Azulay et al., First M87 event horizon telescope results. IV. Imaging the central supermassive black hole. APJl **875**, L4 (2019). arXiv:1906.11241
9. Event Horizon Telescope Collaboration, K. Akiyama, A. Alberdi, W. Alef, K. Asada, R. Azulay et al., First M87 event horizon telescope results. V. Physical origin of the asymmetric ring. APJl **875**, L5 (2019). arXiv:1906.11242
10. L. Barack et al., Black holes, gravitational waves and fundamental physics: a roadmap. Class. Quantum Gravity **36**, 143001 (2019)
11. A.G. Riess et al., Observational evidence from supernovae for an accelerating universe. Astron. J. **116**, 1009 (1998)
12. V.C. Rubin, W.K. Ford, Extended rotation curves of high-luminosity spiral galaxies. IV. Astrophys. J. **225**, L107 (1978)
13. G. t'Hooft, M. Veltman, One-loop divergencies in the theory of gravitation. Ann. Inst. H. Poincare **20**, 69 (1974)
14. T.P. Sotiriou, V. Faraoni, $f(r)$ theories of gravity. Rev. Mod. Phys. **82**, 451 (2010)
15. Y. Fujii, K. Maeda, *The Scalar-Tensor Theory of Gravitation* (Cambridge University Press, Cambridge, 2003)
16. S. Nojiri, S.D. Odintsov, Unified cosmic history in modified gravity: from f(r) theory to Lorentz non-invariant models. Phys. Rep. **505**, 59 (2011)
17. T. Harko et al., $f(r,t)$ gravity. Phys. Rev. D **84**, 024020 (2011)
18. M. Srivastava, S. Shankaranarayanan, Non-trivial quantum fluctuations in asymptotically non-flat black-hole space-times (2020). arXiv:2008.00429
19. M. Partanen, J. Tulkki, Gravity generated by four one-dimensional unitary gauge symmetries and the standard model. Rep. Prog. Phys. **88**, 057802 (2025)
20. S.W. Hawking, Particle creation by black holes. Commun. Math. Phys. **43**, 199–220 (1975)
21. A. Strominger, C. Vafa, Microscopic origin of the Bekenstein–Hawking entropy. Phys. Lett. B **379**, 99–104 (1996)
22. A. Ashtekar, M. Bojowald, Black hole evaporation: a paradigm. Class. Quantum Gravity **22**, 3349 (2005). arXiv:gr-qc/0504029
23. P. Nicolini et al., Noncommutative geometry inspired Schwarzschild black hole. Phys. Lett. B **632**, 547–551 (2006)
24. R.J. Adler, P. Chen, D.I. Santiago, The generalized uncertainty principle and black hole remnants. Gen. Relativ. Gravit. **33**, 2101 (2001). arXiv:gr-qc/0106080
25. A.F. Ali, S. Das, E.C. Vagenas, Discreteness of space from the generalized uncertainty principle. Phys. Lett. B **678**, 497 (2009). arXiv:0906.5396
26. M. Reuter, Nonperturbative evolution equation for quantum gravity. Phys. Rev. D **57**, 971–985 (1998)
27. J.F. Donoghue, General relativity as an effective field theory: the leading quantum corrections. Phys. Rev. D **50**, 3874–3888 (1994)
28. G. Cognola et al., One-loop $f(r)$ gravity in de sitter universe. J. Cosmol. Astropart. Phys. **2005**, 010 (2005)

29. Y. Gim, W. Kim, Thermodynamic phase transition in the rainbow Schwarzschild black hole. J. Cosmol. Astropart. Phys. **2015**, 003 (2015)
30. P. Bargueño, R. Di Criscienzo, M. Nadalini, Quasinormal modes and quantum corrected black holes. Ann. Phys. **413**, 168060 (2020)
31. L. Modesto, Loop quantum black hole. Class. Quantum Gravity **23**, 5587–5602 (2006)
32. C.G. Boehmer, K. Vandersloot, Stability of the Schwarzschild interior in loop quantum gravity. Phys. Rev. D **76**, 104030 (2008)
33. A. Ashtekar, J. Olmedo, P. Singh, Quantum extension of the Kruskal spacetime. Phys. Rev. D **98**, 126003 (2018)
34. G. Mustafa, E. Demir, F. Javed, S. Maurya, E. Güdekli, S. Murodov et al., Epicyclic oscillations and particle collision with trajectories around quantum corrected black holes. Phys. Dark Univ. **46** (2024)
35. A. Ashraf, A. Bouzenada, S. Maurya, F. Atamurotov, P. Channuie, A. Abd-Elmonem et al., Imprints of quantum gravity on periastron precession and trajectories around a black hole. Phys. Dark Univ. **47**, 101787 (2025)
36. G. Mustafa, S.G. Ghosh, O. Donmez, S.K. Maurya, S. Orzuev, F. Atamurotov, Testing Quantum-Corrected Black Holes with QPOs Observations: A Study of Particle Dynamics and Accretion Flow (2025). arXiv:2506.16405
37. K. Nozari, S.H. Mehdipour, Quantum gravity corrections to Schwarzschild black hole thermodynamics. Class. Quantum Gravity **25**, 175015 (2008)
38. F. Ahmed, A. Al-Badawi, I. Sakallı, Exploring geodesics, quantum fields and thermodynamics of schwarzschild-ads black hole with a global monopole in non-commutative geometry. Nucl. Phys. B **1017**, 116951 (2025)
39. K. Jusufi, M. Jamil, P.H.R.S. Moraes, Quasi-periodic oscillations of a gup modified kerr black hole and the possibility of constraining quantum gravity parameters. Eur. Phys. J. C **80**, 354 (2020)
40. S. Das, E.C. Vagenas, Phenomenological implications of the generalized uncertainty principle. Can. J. Phys. **87**, 233–240 (2018)
41. K. Jusufi, M. Azreg-Aïnou, M. Jamil, T. Zhu, Constraining the generalized uncertainty principle through black hole shadow, S2 star orbit, and quasiperiodic oscillations. Int. J. Geom. Methods Mod. Phys. **19**, 2250068 (2022). arXiv:2008.09115
42. J. Abedi, H. Arfaei, Observal signatures of black holes in loop quantum gravity. J. Cosmol. Astropart. Phys. **2016**, 042 (2016)
43. I. Banerjee, Testing black holes in non-linear electrodynamics from the observed quasi-periodic oscillations. JCAP **2022**, 034 (2022). arXiv:2203.10890
44. S.E. Motta, T.M. Belloni, Rethinking the 67 Hz QPO in GRS 1915+105: type-C QPOs at the innermost stable circular orbit (2023). arXiv:2307.00867
45. C.-Y. Shao, C. Zhang, W. Zhang, C.-G. Shao, Scalar fields around a loop quantum gravity black hole in de Sitter spacetime: quasinormal modes, late-time tails and strong cosmic censorship. PRD **109**, 064012 (2024). arXiv:2309.04962
46. K. Nozari, S.H. Mehdipour, Quantum gravity corrections and the classical tests of general relativity. Astrophys. Space Sci. **339**, 581–586 (2012)
47. P. Nicolini, Noncommutative black holes, the final appeal to quantum gravity: a review. Int. J. Mod. Phys. A **24**, 1229–1308 (2019)
48. J. Rayimbaev, A.H. Bokhari, B. Ahmedov, Quasiperiodic oscillations from noncommutative inspired black holes. Class. Quantum Gravity **39**, 075021 (2022)
49. F. Banyuls, J.A. Font, J.M. Ibáñez, J.M. Martí, J.A. Miralles, Numerical 3 + 1 general relativistic hydrodynamics: a local characteristic approach. APJ **476**, 221 (1997)
50. O. Dönmez, Code development of three-dimensional general relativistic hydrodynamics with amr (adaptive-mesh refinement) and results from special and general relativistic hydrodynamics. APSS **293**, 323 (2004). arXiv:gr-qc/0406073
51. O. Donmez, Solution of the 1d special relativistic hydrodynamics(srh) equations using different numerical method and results from different test problems. AM&C **181**, 256 (2006). arXiv:gr-qc/0512104
52. J.A. Font, Numerical hydrodynamics in general relativity. Living Rev. Relativ. **3**, 2 (2000). arXiv:gr-qc/0003101
53. A. Vachher, S.G. Ghosh, Strong gravitational lensing by rotating quantum-corrected black holes: Insights and constraints from EHT observations of M87* and Sgr A*. J. High Energy Astrophys. **45**, 75 (2025). arXiv:2410.11332
54. H. Ali, S.U. Islam, S.G. Ghosh, Shadows and parameter estimation of rotating quantum corrected black holes and constraints from EHT observation of M87* and Sgr A*. J. High Energy Astrophys. **47**, 100367 (2025). arXiv:2410.09198
55. J.-Q. Guo, P.S. Joshi, R. Narayan, L. Zhang, Accretion disks around naked singularities. Class. Quantum Gravity **38**, 035012 (2021). arXiv:2011.06154
56. H. Bondi, F. Hoyle, On the mechanism of accretion by stars. MNRAS **104**, 273 (1944)
57. H. Bondi, On spherically symmetrical accretion. MNRAS **112**, 195 (1952)
58. R. Edgar, A review of Bondi–Hoyle–Lyttleton accretion. NAR **48**, 843 (2004). arXiv:astro-ph/0406166
59. S.E. Motta, T. Belloni, L. Stella, G. Pappas, J. Casares, A.T. Muñoz-Darias et al., Black hole mass and spin measurements through the relativistic precession model: XTE J1859+226. MNRAS **517**, 1469 (2022). arXiv:2209.10376
60. S. Chatterjee, S. Mondal, P. Basu, Vertical equilibrium model for accretion flow: an exact general relativistic self-consistent analysis. Astrophys. J. **941**, 131 (2022)
61. O. Dönmez, Relativistic simulation of flip-flop instabilities of Bondi–Hoyle accretion and quasi-periodic oscillations. MNRAS **426**, 1533 (2012)
62. M. Machida, R. Matsumoto, Excitation of low-frequency qpos in black-hole accretion flows. PASJ **60**, 613 (2008). arXiv:0802.3779
63. B.T. Ferreira, G.I. Ogilvie, On an excitation mechanism for trapped inertial waves in discs around black holes. MNRAS **386**, 2297 (2008). arXiv:0803.1671
64. S.I. Aoki, S. Koide, T. Kudoh, K. Nakayama, K. Shibata, Quasi-periodic inward shock formations in the system of a black hole and an accretion disk and application to quasi-periodic oscillations in galactic black hole candidates. Astrophys. J. **610**, 897 (2004)
65. B.W. Thomson, Determining the origin and possible mechanisms of QPOS in x-ray emissions of neutron stars and black holes Ph.D. thesis, University of North Dakota (2014)
66. F. Koyuncu, O. Dönmez, Numerical simulation of the disk dynamics around the black hole: Bondi–Hoyle accretion. Mod. Phys. Lett. A **29**, 1450115 (2014)
67. O. Donmez, Proposing a physical mechanism to explain various observed sources of QPOs by simulating the dynamics of accretion disks around the black holes. Eur. Phys. J C **84**, 524 (2024). arXiv:2311.08388
68. L. Stella, M. Vietri, Lense-thirring precession and quasi-periodic oscillations in low-mass x-ray binaries. APJl **492**, L59 (1998). arXiv:astro-ph/9709085
69. F. Oktariani, A.T. Okazaki, S. Kato, Excitation of trapped g-mode oscillations in warped disks around black holes. PASJ **62**, 709 (2010). arXiv:1004.0555
70. S. Kato, Trapped, two-armed, nearly vertical oscillations in disks with toroidal magnetic fields II: effects of finite thickness. PASJ **64**, 78 (2012). arXiv:1202.0115

71. S. Chaty, Diskoseismology of accretion disks, in *Extraterrestrial Seismology*, ed. by V.C.H. Tong and R.A. García, pp. 227–237 (Cambridge University Press, 2015)
72. M. Cadoni, M. Oi, A.P. Sanna, Effective models of nonsingular quantum black holes PRD **106**, 024030 (2022). arXiv:2204.09444
73. S. Yang, Y.-P. Zhang, T. Zhu, L. Zhao, Y.-X. Liu, Gravitational waveforms from periodic orbits around a quantum-corrected black hole. JCAP **2025**, 091 (2025). arXiv:2407.00283
74. L. Zhao, M. Tang, Z. Xu, The lensing effect of quantum-corrected black hole and parameter constraints from EHT observations. Eur. Phys. J. C **84**, 971 (2024). arXiv:2403.18606
75. R.C. Pantig, G. Lambiase, A. Övgün, N.J.L.S. Lobos, Spacetime-curvature induced uncertainty principle: Linking the large-structure global effects to the local black hole physics. Phys. Dark Univ. **47**, 101817 (2025). arXiv:2412.00303
76. M. Saleh, B.T. Bouetou, T.C. Kofane, Quasinormal modes of a quantum-corrected Schwarzschild black hole: gravitational and Dirac perturbations. APSS **361**, 137 (2016). arXiv:1604.00820
77. Z.S. Moreira, H.C.D.L. Junior, L.C.B. Crispino, C.A.R. Herdeiro, Quasinormal modes of a holonomy corrected Schwarzschild black hole. PRD **107**, 104016 (2023). arXiv:2302.14722
78. N.I. Shakura, R.A. Sunyaev, Black holes in binary systems. Observational appearance.. AAP **24**, 337 (1973)
79. O. Dönmez, O. Zanotti, L. Rezzolla, On the development of quasi-periodic oscillations in Bondi–Hoyle accretion flows. MNRAS **412**, 1659 (2011). arXiv:1010.1739
80. A. Cruz-Osorio, L. Rezzolla, Common-envelope dynamics of a Stellar-mass black hole: general relativistic simulations. APJ **894**, 147 (2020). arXiv:2004.13782
81. A. Cruz-Osorio, L. Rezzolla, F.D. Lora-Clavijo, J.A. Font, C. Herdeiro, E. Radu, Bondi-Hoyle-Lyttleton accretion onto a rotating black hole with ultralight scalar hair. JCAP **2023**, 057 (2023). arXiv:2301.06564
82. O. Dönmez, Bondi-Hoyle-Lyttleton accretion around the rotating hairy Horndeski black hole. J. Cosmol. Astropart. Phys. **2024**, 006 (2024)
83. H. Gong, S. Li, D. Zhang, G. Fu, J.-P. Wu, Quasinormal modes of quantum-corrected black holes. PRD **110**, 044040 (2024). arXiv:2312.17639
84. R.A. Konoplya, D. Ovchinnikov, B. Ahmedov, Bardeen spacetime as a quantum corrected Schwarzschild black hole: quasinormal modes and Hawking radiation. PRD **108**, 104054 (2023). arXiv:2307.10801
85. C. Liu, H. Siew, T. Zhu, Q. Wu, Y. Sun, Y. Zhao et al., Constraints on the rotating self-dual black hole with quasi-periodic oscillations. JCAP **2023**, 096 (2023). arXiv:2305.12323
86. J. Khodagholizadeh, G. Jafari, A. Allahyari, A. Vahedi, Testing loop quantum gravity by quasi-periodic oscillations: rotating blackholes. Eur. Phys. J. C **84**, 1303 (2024). arXiv:2412.16625
87. O. Dönmez, On the development of the Papaloizou–Pringle instability of the black hole-torus systems and quasi-periodic oscillations. MNRAS **438**, 846 (2014). arXiv:1304.0584
88. O. Donmez, Angular velocity perturbations inducing the Papaloizou-Pringle instability and QPOs in the torus around the black hole. Mod. Phys. Lett. A **32**, 1750108 (2017). arXiv:1703.08175
89. O. Donmez, Dynamical evolution of the shock cone around 4D Einstein-Gauss Bonnet rotating black hole. Phys. Lett. B **827**, 136997 (2022). arXiv:2103.03160
90. O. Donmez, F. Dogan, T. Sahin, Study of asymptotic velocity in the Bondi–Hoyle accretion flows in the domain of Kerr and 4-D Einstein–Gauss–Bonnet gravities. Universe **8**, 458 (2022). arXiv:2205.14382
91. O. Donmez, F. Dogan, Estimating the possible qpos of m87* from the parameters of a hairy kerr black hole. Phys. Dark Univ. **46**, 101718 (2024). arXiv:2407.01478
92. O. Donmez, From low- to high-frequency QPOs around the non-rotating hairy Horndeski black hole: microquasar GRS 1915+105. J. High Energy Astrophys. **45**, 1 (2025). arXiv:2408.10102
93. O. Donmez, Perturbing the stable accretion disk in Kerr and 4D Einstein–Gauss–Bonnet gravities: comprehensive analysis of instabilities and dynamics. Res. Astron. Astrophys. **24**, 085001 (2024). arXiv:2310.13847
94. O. Donmez, F. Dogan, The shock cone instabilities and quasi-periodic oscillations around the Hartle-Thorne black hole. Universe **10**, 152 (2024)
95. S. Karino, Oscillating wind accretion due to x-ray inhibition of line-driven mechanism. Publ. Astron. Soc. Japan **77**, 328 (2025). https://academic.oup.com/pasj/article-pdf/77/2/328/61746257/psae119.pdf
96. B.F. Liu, F. Meyer, E. Meyer-Hofmeister, Spectral state transitions in low-mass x-ray binaries—the effect of hard and soft irradiation. AAP **442**, 555 (2005). arXiv:astro-ph/0506444
97. S.W. Allen, R.J.H. Dunn, A.C. Fabian, G.B. Taylor, C.S. Reynolds, The relation between accretion rate and jet power in x-ray luminous elliptical galaxies. Mon. Not. R. Astron. Soc. **372**, 21 (2006). https://academic.oup.com/mnras/article-pdf/372/1/21/5776385/mnras0372-0021.pdf
98. M. Hakan Erkut, S. Duran, O. Catmabacak, O. Catmabacak, A new correlation with lower kilohertz quasi-periodic oscillation frequency in the ensemble of low-mass x-ray binaries. Astrophys. J. **831**, 25 (2016)
99. L. Landau, E. Lifshitz, *Mechanics, 1* (Pergamon Press, Oxford, 1976)
100. R.A. Remillard, J.E. McClintock, X-ray properties of black-hole binaries. ARAA **44**, 49 (2006). arXiv:astro-ph/0606352
101. R.A. Remillard, J.E. McClintock, J.A. Orosz, A.M. Levine, The x-ray outburst of h1743–322 in 2003: high-frequency qpos with a 3:2 frequency ratio. APJ **637**, 1002 (2006). arXiv:astro-ph/0407025
102. K. Fukumura, D. Kazanas, G. Stephenson, Quasi-periodic oscillations from random x-ray bursts around rotating black holes. Astrophys. J. **695**, 1199 (2009)
103. K.L. Smith, C.R. Tandon, R.V. Wagoner, Confrontation of observation and theory: high-frequency qpos in x-ray binaries, tidal disruption events, and active galactic nuclei. APJ **906**, 92 (2021). arXiv:2011.05346
104. H. Zhang, L. Meng, L. Zhang, B. Dai, Revisiting the observation-theory confrontation in high-frequency QPOs: a new QPO in NGC 5506, intermediate-mass black holes, and the crucial role of accretion state. MNRAS **538**, 2161 (2025). arXiv:2503.03631
105. O. Donmez, Evolution of Shock Structures and QPOs After Halting BHL Accretion onto Kerr Black Hole (2025). arXiv:2503.16665
106. G. Principe, Event Horizon Telescope Multi-Wavelength Working Group, Event Horizon Telescope Collaboration, Fermi-Lat Collaboration, H.E.S.S. Collaboration, MAGIC Collaboration et al., Multi-wavelength view of the M87 black hole captured by event horizon telescope, in *American Astronomical Society Meeting Abstracts*, *American Astronomical Society Meeting Abstracts*, vol. 238, p. 125.03 (2021)
107. Event Horizon Telescope Collaboration, K. Akiyama, A. Alberdi, W. Alef, J.C. Algaba, R. Anantua et al., First Sagittarius A* event horizon telescope results. VI. Testing the black hole metric. APJl **930**, L17 (2022)
108. Event Horizon Telescope Collaboration, Numerical study of astrophysical models of supermassive black holes, in *American Astronomical Society Meeting #240*, *American Astronomical Society Meeting Abstracts*, vol. 240, p. 211.05 (2022)
109. E. Kara, J. García, Supermassive Black Holes in X-rays: From Standard Accretion to Extreme Transients (2025). arXiv:2503.22791

110. H. Gulia, J. Singh, F. Atamurotov, S.G. Ghosh, Observational signatures of shadows in gup-corrected Kerr black holes and constraints from eht data. Phys. Dark Univ. **48**, 101954 (2025)
111. P. Nicolini, Noncommutative black holes, the final appeal to quantum gravity: a review. Int. J. Mod. Phys. A **24**, 1229 (2009). arXiv:0807.1939
112. Z. Kovács, T. Harko, Can accretion disk properties observationally distinguish black holes from naked singularities? PRD **82**, 124047 (2010). arXiv:1011.4127
113. P.S. Joshi, D. Malafarina, R. Narayan, Distinguishing black holes from naked singularities through their accretion disc properties. Class. Quantum Gravity **31**, 015002 (2014). arXiv:1304.7331
114. V. Deliyski, G. Gyulchev, P. Nedkova, S. Yazadjiev, Observing naked singularities with the present and next-generation Event Horizon Telescope. PRD **111**, 064068 (2025). arXiv:2401.14092
115. N. Ortiz, O. Sarbach, T. Zannias, Observational distinction between black holes and naked singularities: the role of the redshift function. Class. Quantum Gravity **32**, 247001 (2015). arXiv:1401.4227
116. A. Markowitz, P. Uttley, Low-luminosity active galactic nuclei as analogs of galactic black holes in the low/hard state: evidence from x-ray timing of ngc 4258. APJl **625**, L39 (2005). arXiv:astro-ph/0504152
117. J. Rodriguez, S. Corbel, E. Kalemci, J.A. Tomsick, M. Tagger, An x-ray timing study of xte j1550–564: evolution of the low-frequency quasi-periodic oscillations for the complete 2000 outburst. Astrophys. J. **612**, 1018 (2004)
118. C. Gao, Z. Yan, W. Yu, Low-frequency quasi-periodic oscillation in MAXI J1820+070: Revealing distinct Compton and reflection contributions. MNRAS **520**, 5544 (2023). arXiv:2302.00915
119. D. Rawat, M. Pahari, J.S. Yadav, P. Jain, R. Misra, K. Bagri et al., Study of timing evolution from nonvariable to structured large-amplitude variability transition in grs 1915 + 105 using astrosat. Astrophys. J. **870**, 4 (2018)
120. H. Sreehari, A. Nandi, S. Das, V.K. Agrawal, S. Mandal, M.C. Ramadevi et al., AstroSat view of GRS 1915+105 during the soft state: detection of HFQPOs and estimation of mass and spin. MNRAS **499**, 5891 (2020). arXiv:2010.03782
121. S. Motta, J. Homan, T. Muñoz Darias, P. Casella, T.M. Belloni, B. Hiemstra, Discovery of two simultaneous non-harmonically related quasi-periodic oscillations in the 2005 outburst of the black hole binary gro j1655–40. MNRAS **427**, 595 (2012). arXiv:1209.0327
122. K.C. Gendreau, Z. Arzoumanian, T. Okajima, The Neutron star Interior Composition ExploreR (NICER): an Explorer mission of opportunity for soft x-ray timing spectroscopy, in *Space Telescopes and Instrumentation 2012: Ultraviolet to Gamma Ray*, ed. by T. Takahashi, S.S. Murray and J.-W.A. den Herder, *Society of Photo-Optical Instrumentation Engineers (SPIE) Conference Series*, vol. 8443, p. 844313 (2012). https://doi.org/10.1117/12.926396